The Fornax Deep Survey with VST. II. Fornax A: A Two-phase Assembly Caught in the Act

E. Iodice[1], M. Spavone[1,2], M. Capaccioli[3], R. F. Peletier[4], T. Richtler[5], M. Hilker[6], S. Mieske[7], L. Limatola[1], A. Grado[1], N. R. Napolitano[1], M. Cantiello[8], R. D'Abrusco[9], M. Paolillo[10], A. Venhola[11], T. Lisker[12], G. Van de Ven[13], J. Falcon-Barroso[14], and P. Schipani[1,15]

[1] INAF—Astronomical Observatory of Capodimonte, via Moiariello 16, Naples, I-80131, Italy; iodice@na.astro.it
[2] Astronomical Observatory of Capodimonte, via Moiariello 16, Naples, I-80131, Italy
[3] University of Naples "Federico II," C.U. Monte SantAngelo, Via Cinthia, I-80126, Naples, Italy
[4] Kapteyn Astronomical Institute, University of Groningen, P.O. Box 72, 9700 AV Groningen, The Netherlands
[5] Universidad de Concepción, Concepción, Chile
[6] European Southern Observatory, Karl-Schwarzschild-Strasse 2, D-85748 Garching bei Munchen, Germany
[7] European Southern Observatory, Alonso de Cordova 3107, Vitacura, Santiago, Chile
[8] INAF—Astronomical Observatory of Teramo, Via Maggini, I-64100, Teramo, Italy
[9] Smithsonian Astrophysical Observatory/Chandra X-Ray Center, Cambridge, MA 02138, USA
[10] Univ. of Naples "Federico II," C.U. Monte SantAngelo, Via Cinthia, I-80126, Naples, Italy
[11] Division of Astronomy, Department of Physics, University of Oulu, Oulu, Finland
[12] Zentrum fuer Astronomie der Universitaet Heidelberg, Germany
[13] Max Planck Institute for Astronomy, Heidelberg, Germany
[14] Instituto de Astrofísica de Canarias, C/ Via Láctea s/n, E-38200 La Laguna, Canary Islands, Spain
[15] Astron. Observatory of Capodimonte, via Moiariello 16, Naples, I-80131, Italy

Abstract

As part of the Fornax Deep Survey with the ESO VLT Survey Telescope, we present new g- and r-band mosaics of the SW group of the Fornax Cluster. It covers an area of 3×2 square degrees around the central galaxy NGC 1316. The deep photometry, the high spatial resolution of OmegaCam, and the large covered area allow us to study the galaxy structure, trace stellar halo formation, and look at the galaxy environment. We map the surface brightness profile out to $33'$ (~ 200 kpc $\sim 15 R_e$) from the galaxy center, down to $\mu_g \sim 31$ mag arcsec^{-2} and $\mu_r \sim 29$ mag arcsec^{-2}. This allow us to estimate the scales of the main components dominating the light distribution, which are the central spheroid, inside $5.'5$ (~ 33 kpc), and the outer stellar envelope. Data analysis suggests that we are catching in the act the second phase of the mass assembly in this galaxy, since the accretion of smaller satellites is going on in both components. The outer envelope of NGC 1316 still hosts the remnants of the accreted satellite galaxies that are forming the stellar halo. We discuss the possible formation scenarios for NGC 1316, by comparing the observed properties (morphology, colors, gas content, kinematics, and dynamics) with predictions from cosmological simulations of galaxy formation. We find that (i) the central spheroid could result from at least one merging event (it could be a preexisting early-type disk galaxy with a lower-mass companion) and (ii) the stellar envelope comes from the gradual accretion of small satellites.

Key words: galaxies: clusters: individual (NGC 1316) – galaxies: elliptical and lenticular, cD – galaxies: formation – galaxies: halos – galaxies: photometry

1. Introduction

The hierarchical structure formation at all scales is one of the strongest predictions of the ΛCDM model. In this framework, clusters of galaxies are expected to grow over time by accreting smaller groups. The galaxies at the center of the clusters continue to undergo active mass assembly, and in this process, gravitational interactions and merging among systems of comparable mass and/or smaller objects play a fundamental role in defining the observed structures. Since timescales in the outer parts are long, the imprints of mass assembly that we are currently observing are seen there: these are the regions of the stellar halo. This is an extended, diffuse, and very faint ($\mu \sim 26$–27 mag arcsec^{-2} in the g band) component made of stars stripped from satellite galaxies, in the form of streams and tidal tails, with multiple stellar components and complex kinematics, which is still growing at the present epoch. On the scale of the cluster, during the infall of groups of galaxies to form the cluster, the material stripped from the galaxy outskirts builds up the intracluster light (ICL; De Lucia & Blaizot 2007;

Puchwein et al. 2010; Cui et al. 2014). This is a diffuse faint component that grows over time with the mass assembly of the cluster, to which the relics of the interactions among galaxies (stellar streams and tidal tails) also contribute, growing over time with the mass assembly of the cluster (see Arnaboldi & Gerhard 2010; Tutukov & Fedorova 2011; Mihos 2015, for reviews).

From the theoretical side, semianalytic models combined with cosmological N-body simulations have become very sophisticated, with detailed predictions about the structure of stellar halos, the ICL formation, and the amount of substructures in various kinds of environment (e.g., Martel et al. 2012; Watson et al. 2012; Cooper et al. 2013, 2015b; Contini et al. 2014; Pillepich et al. 2014, and references therein).

Rich environments of galaxies, i.e., groups and clusters, are therefore the appropriate sites to study the mass assembly processes that lead to the observed galaxy structure, stellar halos, and ICL, in order to test hierarchical formation theories at all scales. In recent years, the advent of deep imaging

surveys allows us to study galaxy structures down to the faintest surface brightness levels and out to large distances from the galaxy center to map stellar halos and the ICL (Mihos et al. 2005, 2016; Janowiecki et al. 2010; Martínez-Delgado et al. 2010; Roediger et al. 2011; Ferrarese et al. 2012; van Dokkum et al. 2014; Capaccioli et al. 2015; Duc et al. 2015; Munoz et al. 2015; Trujillo & Fliri 2016; Crnojević et al. 2016; Iodice et al. 2016; Merritt et al. 2016; Spavone et al. 2017).

The Fornax Deep Survey (FDS) is just a part of this campaign. FDS is a multiband (u, g, r, and i) imaging survey at the VLT Survey Telescope (VST) that aims to cover the whole Fornax Cluster out to the virial radius ($\sim$0.7 Mpc; Drinkwater et al. 2001), with an area of about 26 square degrees around the central galaxy NGC 1399 in the cluster core. The Fornax Cluster is the second most massive galaxy concentration within 20 Mpc, after the Virgo Cluster, and it is among the richest nearby targets to study galaxy evolution and dynamical harassment in dense environments. Recent works indicate that it has a complex structure and the mass assembly is still ongoing. The core is in a quite evolved phase (Grillmair et al. 1994; Jordán et al. 2007), since most of the bright ($m_B < 15$ mag) cluster members are early-type galaxies (Ferguson 1989), more than in the Virgo Cluster. It hosts a vast population of dwarf galaxies and ultracompact galaxies (Hilker 2015; Munoz et al. 2015; Schulz et al. 2016) and an intracluster population of globular clusters (GCs; Schuberth et al. 2010; D'Abrusco et al. 2016) and planetary nebulae (PNs; Napolitano et al. 2003; McNeil-Moylan et al. 2012). Dynamics on the large scale shows that a poor subgroup of galaxies on the SW is falling into the cluster core along a cosmic web filament (Drinkwater et al. 2001; Scharf et al. 2005). The FDS also includes such an infalling structure of the Fornax Cluster. Therefore, the FDS will provide an unprecedented view of structures of galaxies, ranging from giant early-type galaxies to small spheroidal galaxies; a full characterization of small stellar systems around galaxies, such as GCs and ultracompact dwarf galaxies; and, on the cluster scale, hints on the galaxy evolution as a function of the environment.

First results have provided the mosaic of 3×2 square degrees around the central galaxy NGC 1399.[16] The deep imaging allows us to map the surface brightness out to a distance of $\sim$200 kpc ($R \sim 6R_e$) from the center of NGC 1399 and down to $\mu_g \simeq 31$ mag arcsec^{-2} (Iodice et al. 2016). In the intracluster region, on the west side of NGC 1399 and toward NGC 1387, we have detected a faint ($\mu_g \sim 29$–30 mag arcsec^{-2}) stellar bridge, about $5'$ long ($\sim$29 kpc), which could be due to the ongoing interaction between the two galaxies, where the outer envelope of NGC 1387 on its east side is stripped away. By using about 3000 candidate GCs extracted from the VST $ugri$ images covering the central $\sim$8.4 deg^2 of the cluster, D'Abrusco et al. (2016) traced the spatial distribution of candidate GCs in a region of $\sim$0.5 deg^2 within the core of the Fornax Cluster. In particular, they confirmed the bridge between NGC 1399 and NGC 1387, finding an overdensity of blue GCs in this region, as previously suggested by Bassino et al. (2006).

The FDS observations are planned to be completed by the end of 2017. A full description of the data will be presented soon in a forthcoming paper. In this current work, we focus on a new mosaic of the SW group of the Fornax Cluster, in the g and r bands, which covers an area of 3×2 square degrees

---

[16] See the ESO photo release at https://www.eso.org/public/news/eso1612/.

around the central galaxy NGC 1316 (see Figure 1). In the following, we adopt a distance for NGC 1316 of $D = 20.8 \pm 0.5$ Mpc (Cantiello et al. 2013), which yields an image scale of 101 parsec/arcsec.

2. A Literature Review of NGC 1316

NGC 1316, also known as Fornax A, is one of the most fascinating giant galaxies in the local universe. It is the brightest member of the Fornax Cluster located in the subgroup to the SW of the cluster (Drinkwater et al. 2001), at about $4°$ ($\sim$1.5 Mpc) from NGC 1399. Over the past few years, NGC 1316 has been widely studied in a large wavelength range. The results are summarized in this section. The main observed properties show a very complex structure for this galaxy and point toward a rich history of interaction events.

Morphology and structure in the optical and infrared: NGC 1316 resembles an elongated spheroid characterized by pronounced and extended dust patches, more concentrated in the galaxy center and best mapped by *Hubble Space Telescope* images (Carlqvist 2010), and several ripples and loops, with different shape and luminosity (see Figure 2). The first detailed description of all the substructures in NGC 1316 was given by Schweizer (1980), based on wide-field photographic plates. In particular, he pointed out the giant L5 loop on the SW regions of the galaxy outskirt and an elongated feature dubbed "plume" inside the galaxy, on the NW (see Figure 2). Besides, Schweizer (1980) detected an inner rotating disk of ionized gas, along the minor axis of the galaxy, and a giant H II region south of the center. In a region where there is no evident sign of ongoing star formation, at a distance of $6'$ from the center, Mackie & Fabbiano (1998) found an extended ($\sim$1$'$.5) emission line region (EELR). In the nucleus of the galaxy there is a kinematically decoupled cold stellar disk and a spiral-like structure of gas at about 5–15$''$ from the center (Beletsky et al. 2011). The *Spitzer* images (at 8.0 μm) map the morphology of the dust emission in the inner $3'$, displaying a bar-like structure along the galaxy minor axis ending with spiral arms, most pronounced on the NW side (see Figure 3 of Lanz et al. 2010). Duah Asabere et al. (2016) suggested that the dust in this galaxy has an external origin, coming from a recent infall and disruption of one or more smaller gas-rich galaxies. From the *Spitzer* images, Lanz et al. (2010) estimated that the merger late-type galaxy had a stellar mass of $\sim$10^{10} $M_\odot$ and an amount of gas of $\sim$10^9 $M_\odot$.

Emission from NGC 1316: The amount of gas in NGC 1316 is quite small. Horellou et al. (2001) found $\sim$5 $\times$ 10^8 $M_\odot$ of molecular gas inside 2$'$, which is mainly associated with dust. The galaxy is devoid of neutral atomic gas to a limiting mass of $\sim$10^8 $M_\odot$, while some emission is detected in four clumps in the galaxy outskirts. Two of these coincide with the H II region and the EELR in the south (Schweizer 1980; Mackie & Fabbiano 1998; Richtler et al. 2012), and two others are on the NW side. The total gas-to-stellar mass ratio in NGC 1316 is $\sim$10^{-4}.

The X-ray emission of NGC 1316 was mapped with most of the X-ray satellites (Fabbiano et al. 1992; Feigelson et al. 1995; Iyomoto et al. 1998; Kim et al. 1998; Kim & Fabbiano 2003; Konami et al. 2010). As shown by Mackie & Fabbiano (1998, see Figure 6 of that paper), the main contributions to the X-ray emission are with the galaxy center and with two of the most luminous substructures in the light, dubbed by Schweizer (1980) as L1 in the south and L2 on the east of the galaxy (see
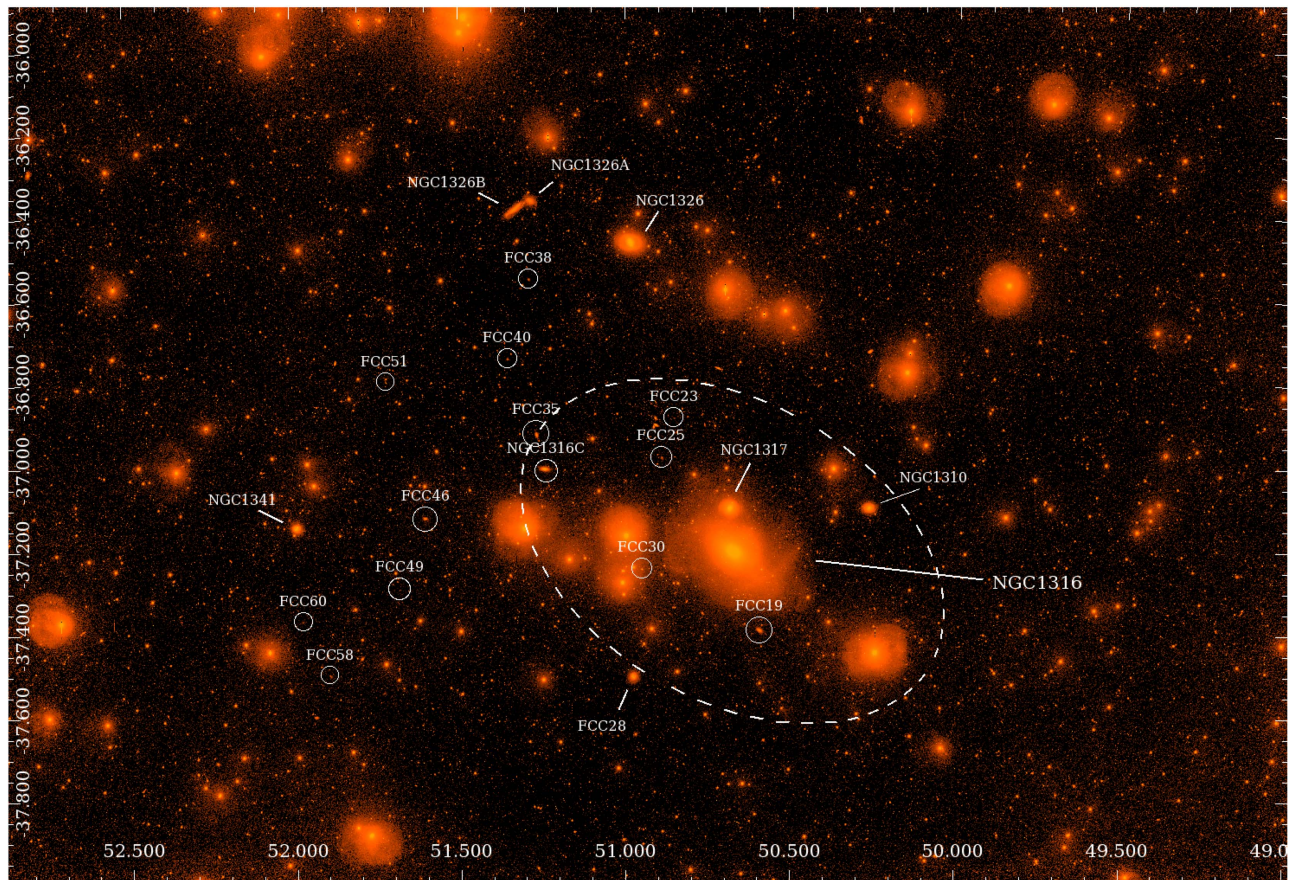
Figure 1. Sky-subtracted VST mosaic in the r band of the central 3.6×2.1 deg^2 around NGC 1316, which is the brightest object in the center. All the galaxy members of this subgroup of the Fornax Cluster (Ferguson 1989) are also indicated, including the dwarf candidates (inside the white circles). R.A. and decl. (in degrees) are reported on the horizontal and vertical axes, respectively.

Figure 2). There is an elongated region of X-ray emission to the NW of NGC 1316, corresponding to the region of the plume.

In the radio domain, NGC 1316 is the third-brightest nearby galaxy ($L_{\rm radio} = 259$ Jy), after NGC 5128 (Centaurus A) and M87 (Ekers et al. 1983), within 20 Mpc. At a position angle of $110°$, $30°$ away from the galaxy rotation axis, there are prominent radio lobes, spanning $33'$, made by polarized filaments (Fomalont et al. 1989). In addition to the radio lobes, there is also an S-shaped nuclear radio jet (Geldzahler & Fomalont 1984). A low-level emission bridge is detected between the two lobes, but it is displaced by about $8'$ from the center of the galaxy. The authors claim that the offset bridge, which is unusual in radio galaxies, could be the remnant of the original bridge, formed with the lobes and aligned with them but disrupted by an infalling galaxy. From combined *Spitzer*, *Chandra*, *XMM-Netwton*, and VLA observations for NGC 1316, Lanz et al. (2010) gave a detailed description and formation of the radio lobes and X-ray cavities.

Globular cluster system: The GCs of NGC 1316 have been studied in detail over the past 10 years, suggesting the presence of a complex GC system in terms of age and metallicity (Goudfrooij 2012; Richtler et al. 2012, and references therein). Recent results by Sesto et al. (2016) indicate that the GC system in NGC 1316 is made by four stellar cluster populations with different ages, abundances, and spatial distributions. Two of them have similar characteristics to the GCs observed in early-type galaxies. The dominant GC component has an intermediate-age stellar population (~ 5 Gyr), and the younger GC population is about 1 Gyr. The presence of an intermediate-age stellar population was also pointed out by Cantiello et al. (2013) by studying the surface brightness fluctuations in NGC 1316.

Stellar kinematics and dynamics: The stellar kinematics in NGC 1316 indicate that the rotation velocity along the major axis increases to 150–170 km s^{-1} at $R \sim 90''$ and decreases to 100 km s^{-1} at larger radii, out to $R \sim 130''$. The velocity dispersion is quite high, being 250 km s^{-1} in the center and decreasing to 150 km s^{-1} at $R \sim 380''$ (Arnaboldi et al. 1998; Bedregal et al. 2006). The amount of rotation derived from the PN kinematics remains almost constant at about 100 km s^{-1} out to $500''$ from the center (McNeil-Moylan et al. 2012). The dynamical models based on both PNs and GCs indicate a high dark matter content, similar to what is found in giant ellipticals (McNeil-Moylan et al. 2012; Richtler et al. 2014).

3. Observations and Data Reduction

The observations presented in this work are part of the ongoing FDS with the ESO VST (see Iodice et al. 2016). FDS is based on two Guaranteed Time Observation surveys, *FOCUS*[17] (P.I. R. Peletier) and *VEGAS*[18] (P.I. E. Iodice; Capaccioli et al. 2015).

VST is a 2.6 m wide-field optical survey telescope, located at Cerro Paranal in Chile (Schipani et al. 2012), equipped with the

---

[17] www.astro.rug.nl/fds
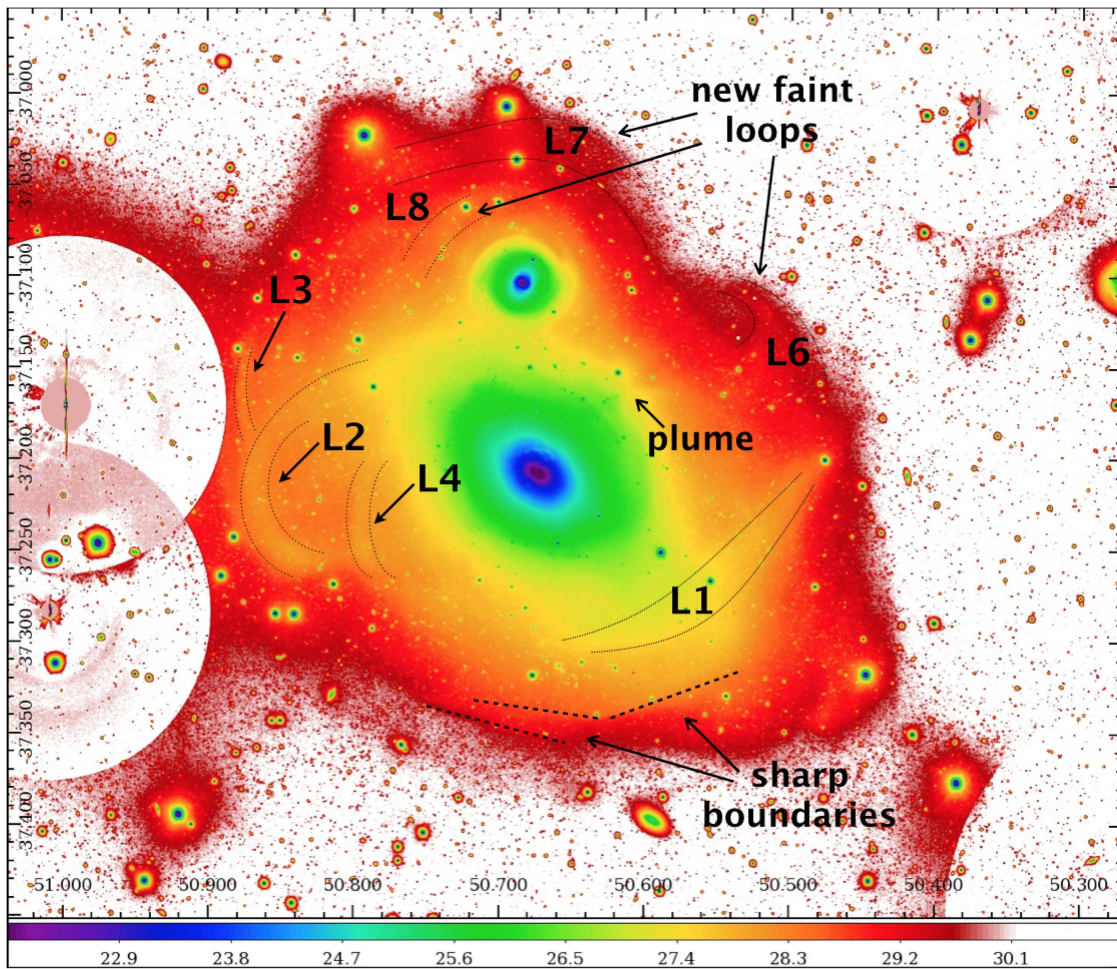[18] http://www.na.astro.it/vegas/VEGAS/Welcome.html

Figure 2. Structure of NGC 1316 as it appears in the *g* band, plotted in surface brightness levels (shown in the color bar). The image size is ∼1 × 0.6 square degrees. The most luminous substructures are marked on the image. The known loops presented by Schweizer (1980) and Richtler et al. (2014) are L1, L2, L3, and L4, while the new and faintest ones found in the deep VST data are on the N–NW. The peculiar sharp boundaries on the S–SE side are delimited by the dashed lines.

wide-field camera OmegaCam, covering the optical wavelength range from 0.3 to 1.0 μm (Kuijken 2011). The field of view of OmegaCam is $1 \times 1 \, \mathrm{deg}^2$, and the mean pixel scale is $0\rlap{.}''21 \, \mathrm{pixel}^{-1}$.

The observations were collected during a visitor mode run from 2015 November 9 to 14 (runID: 096.B-0582(A)). Images were taken in *g* and *r* bands[19] during dark time, in photometric conditions, with an average seeing between 0.6 and $1\rlap{.}''1$. We covered an area of $6 \, \mathrm{deg}^2$ around NGC 1316.

The data were processed with the *VST-Tube* imaging pipeline, whose main steps (pre-reduction, astrometric and photometric calibration, mosaic production) are discussed in detail in Grado et al. (2012) and in Appendix A of Capaccioli et al. (2015).

We used the *step-dither* observing strategy, already adopted for the observations of the core of the Fornax Cluster (Iodice et al. 2016). It consists of a cycle of short exposures (150 s) for each of the six fields acquired in the area of Fornax A. For each field, we obtained 44 exposures in the *g* band and 33 in the *r* bands, giving a total exposure time of 1.83 and 1.37 hr in the *g* and *r* bands, respectively. This observing strategy allows a very accurate estimate of the sky background around bright and

extended galaxies. For the FDS data set presented in this paper, the five (almost empty) fields around that containing NGC 1316 are used as sky frames. Two of them are on the east, two others are on the west, and one more is on the north of NGC 1316. For each night, we derived an average sky frame using these five fields (where all bright sources are masked). The average sky frame is scaled and subtracted off from each science frame. In the first paper of the FDS, Iodice et al. (2016) discussed in detail the possible contributions to the sky brightness (such as galactic cirrus, zodiacal light, and terrestrial airglow) and how to take them into account. The small contribution of the smooth components listed above plus the extragalactic background light to the sky brightness is taken into account by the average sky frame derived for each observing night. In the sky-subtracted science frame only a possible differential component could remain, which contributes to the "residual fluctuations"[20] in the background and sets the accuracy of the sky-subtraction step.

In Figure 1 we show the sky-subtracted VST mosaic in the *g* band of the central $3.6 \times 2 \, \mathrm{deg}^2$ around NGC 1316. For all the Fornax Cluster members in this area, included in the Fornax Cluster Catalog by Ferguson (1989), the integrated magnitudes

---

[20] The residual fluctuations in the sky-subtracted images are the deviations from the background in the science frame with respect to the average sky frame obtained by the empty fields close to the target.

Table 1
Integrated Magnitudes in the g and the $g - r$ Color for the Member Galaxies in the Region of the Fornax Cluster Shown in Figure 1

Object	α h:m:s	δ d:m:s	Morph Type	Radial Velocity (km s^{-1})	r_{30} (arcsec)	m_g (mag)	$g - r$ (mag)
(1)	(2)	(3)	(4)	(5)	(6)	(7)	(8)
NGC 1310	03 21 03.4	−37 06 06	SB	1805	105	12.351 ± 0.004	0.544 ± 0.006
NGC 1316	03 22 41.7	−37 12 30	SAB0	1760	1985	8.43 ± 0.003	0.717 ± 0.005
NGC 1316C	03 24 58.4	−37 00 34	SA	1800	66.15	13.720 ± 0.006	0.51 ± 0.01
NGC 1317	03 22 44.3	−37 06 13	SAB	1941	115.5	11.012 ± 0.003	0.729 ± 0.004
NGC 1326	03 23 56.4	−36 27 53	SB	1360	178.5	10.491 ± 0.003	0.646 ± 0.004
NGC 1326A	03 25 08.5	−36 21 50	SB	1831	63	13.697 ± 0.004	0.378 ± 0.006
NGC 1326B	03 25 20.3	−36 23 06	SB	999	118.65	12.584 ± 0.006	0.29 ± 0.01
NGC 1341	03 27 58.4	−37 09 00	SAB	1876	82.95	11.918 ± 0.003	0.399 ± 0.004
FCC 019	03 22 22.7	−37 23 54	dS0	1407	39.06	15.119 ± 0.007	0.58 ± 0.01
FCC 023	03 23 24.7	−36 53 11	ImV or dE5	...	10.5	19.03 ± 0.02	0.60 ± 0.03
FCC 025	03 23 33.5	−36 58 52	dE0	....	16.8	17.66 ± 0.01	0.54 ± 0.02
FCC 028	03 23 54.2	−37 30 33	SB	....	10.5	13.357 ± 0.004	0.536 ± 0.006
FCC 035	03 25 04.2	−36 55 39	SmIV	1800	36.75	15.028 ± 0.006	0.23 ± 0.01
FCC 038	03 25 09.4	−36 33 07	dS0	....	17.85	17.47 ± 0.01	0.49 ± 0.02
FCC 040	03 25 24.8	−36 44 36	dE4	....	16.8	17.70 ± 0.01	0.56 ± 0.02
FCC 046	03 26 25.0	−37 07 34	dE4	....	37.8	15.354 ± 0.008	0.46 ± 0.01
FCC 049	03 26 43.5	−37 17 51	dE4	....	13.86	19.15 ± 0.03	0.47 ± 0.05
FCC 051	03 26 53.1	−36 47 51	dE4	....	9.87	18.04 ± 0.01	0.33 ± 0.02
FCC 058	03 27 34.6	−37 30 11	dE4	....	17.75	17.79 ± 0.01	0.76 ± 0.02
FCC 060	03 27 54.0	−37 22 27	ImV or dE2	1407	18.48	18.31 ± 0.02	0.35 ± 0.04

Note. Column (1): Fornax Cluster members from Ferguson (1989). Columns (2) and (3): R.A. and decl. Columns (4) and (5): morphological type and heliocentric radial velocity given by NED. Column (6): aperture radius in arcsec corresponding to the surface brightness $\mu_g = 30$ mag arcsec^{-2}. Column (7): integrated magnitude in the g band, derived inside a circular aperture with $r = r_{30}$. Values were corrected for the Galactic extinction by using the absorption coefficient derived according to Schlegel et al. (1998). Column (8): integrated $g - r$ color.

in the g band and the $g - r$ integrated color inside the circular aperture at the radius corresponding to $\mu_g = 30$ mag arcsec^{-2} are listed in Table 1.

The inner structure of NGC 1316 and the faint features in the outer envelope are presented and discussed in the next sections. The surface photometry of all the bright galaxies in this subgroup of the Fornax Cluster is the subject of a forthcoming paper.

4. The Complex Structure of NGC 1316

The structure of NGC 1316 has been widely described in the literature (Schweizer 1980; Mackie & Fabbiano 1998; Richtler et al. 2012, 2014). To date, the VST mosaics in the g (see Figure 1) and r bands cover the most extended area observed around NGC 1316. In this section we describe the morphology and color distribution of NGC 1316, focusing on the new main features revealed by the deep VST images.

4.1. Morphology: The New Faint Features in the Galaxy Outskirts

In Figure 2 we show a smaller region of the g-band mosaic (plotted in surface brightness levels, where the brightest stars are modeled and subtracted), zoomed in on the galaxy center. There are a wealth of loops that characterize the outskirts of NGC 1316, down to surface brightnesses of $\mu_g \sim 30$ mag arcsec^{-2}. Shells and dusty features perturb the inner and luminous regions of the galaxy. We have marked the known loops (L1, L2, L3, L4) and substructures (sharp boundaries and the plume) identified and discussed by Schweizer (1980) and Richtler et al. (2012). In addition to these, the deep VST images allow us to detect at least three more faint loops on the N–NW side of the envelope, at the level of $\mu_g \sim 29$–30 mag arcsec^{-2}, which we named L6, L7, and

L8. Loop L6 in the NW appears as a very curved arc emerging from the bright west edge of L1. The large area covered by the VST mosaic and the large integration time allow us to confirm the presence of the giant loop L5 identified by Schweizer (1980) on the photographic plates, in the SW region (see Figure 3). It extends out to about 0°.44 from the galaxy center, corresponding to a projected distance of about 160 kpc. In addition, we notice a very faint and less extended (15′ ∼91 kpc) loop, protruding from the outer envelope on the NW side of the galaxy, identified as L9 (see Figure 3). The VST images allow us to point out the structure of the SW giant loop L5: it has a filamentary appearance close to the galaxy, while several bright knots dominate the emission on its SE part. On the west side it seems to have a more diffuse structure, but here the light is contaminated by the faint halo of the close bright star. The brightest knots and filaments have r-band surface magnitudes in the range of 29–30 mag arcsec^{-2} (see Figure 3). The NW small loop L9 is even fainter than this.

4.2. The Color Distribution

In Figure 4 (top panel) we show the $g - r$ color map, where we marked the regions of all features identified in NGC 1316 and described in the previous sections.

The $g - r$ map points out two main characteristics in the color distribution: (1) The color map is asymmetric, being redder on the NW side (0.8 mag $\leqslant g - r \leqslant 1$ mag) than the corresponding one on the SE side (0.6 mag $\leqslant g - r \leqslant 0.8$ mag). This was already noticed by Richtler et al. (2014), but on a smaller area close to the center. (2) In correspondence to the sharp boundaries, there is a "sharp" change also in the color, where southern parts are redder. On the north, the color map shows that stars and dust in the close companion NGC 1317 follow an unperturbed spiral structure and the disk appears intact. As already stressed by
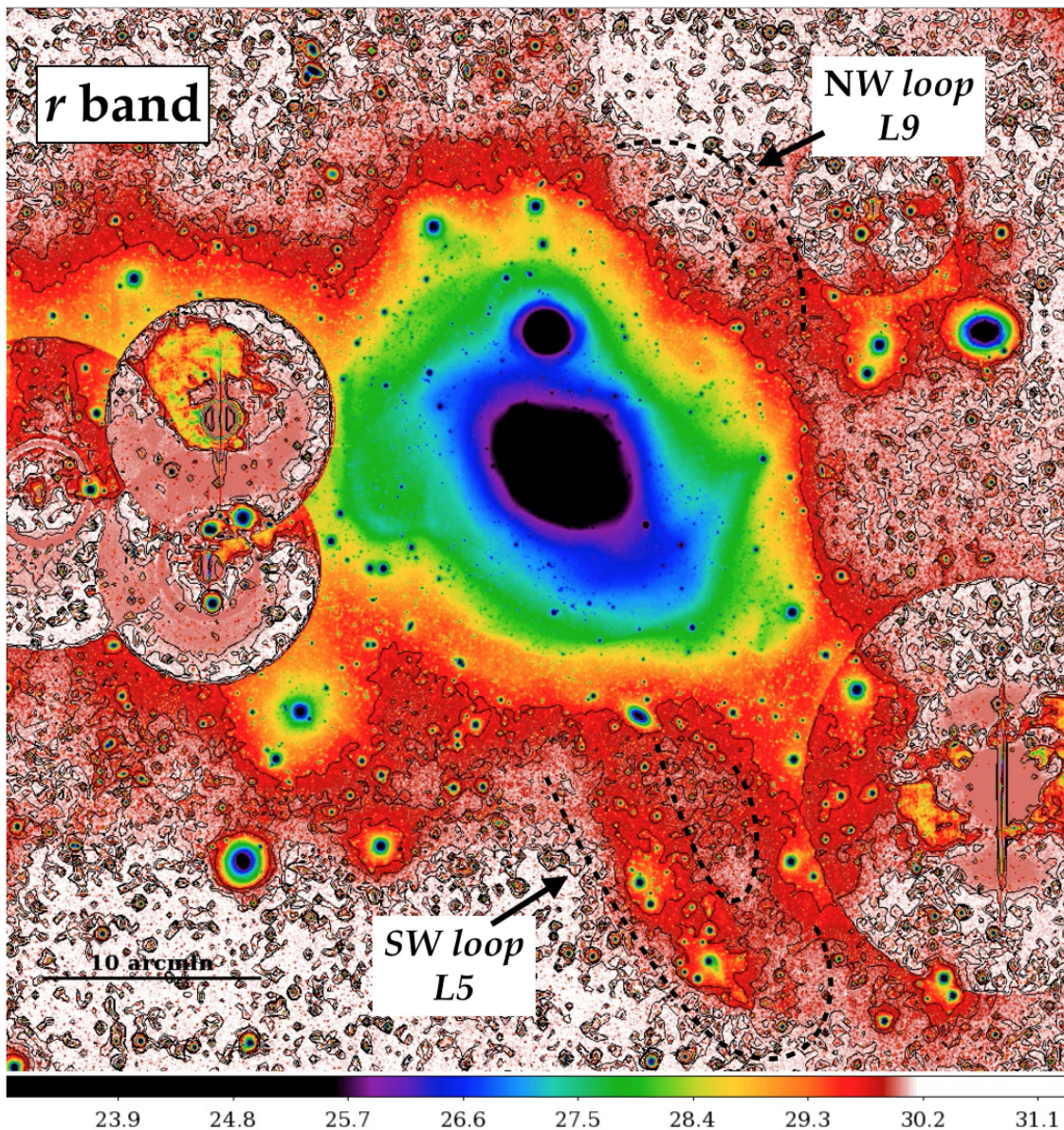
Figure 3. Enlarged regions of the mosaic shown in Figure 1, of about 1×1 square degrees around NGC 1316 in r band, plotted in surface brightness levels (shown in the color bar). Black lines are the following surface brightness levels: 29.65, 29.9, 30.05, and 30.1 mag arcsec^{-2}. The brightest parts of close stars were subtracted off. The extended loop in the SW area (L5) and the new faint loop on the NW (L9) are marked in the image.

Richtler et al. (2014), this suggests that, even if the two galaxies appear very close in projection, an interaction between them can be reasonably excluded. The color distribution of the giant SW loop L5 is mapped for the first time. Differently from what we observed for the outermost loops (L2, L6, L7, and L8), L5 is redder, with average color similar to the inner region of the galaxy. There are two extended areas of L5, close to the bright knots identified in the light distribution that have $0.69 \, \mathrm{mag} \leqslant g - r \leqslant 0.78$ mag.

The center of the galaxy is very red, with $g - r \sim 0.8$ mag. For $R \geqslant 3'$, the average color is $g - r \sim 0.65$ mag, and it is bluer, down to 0.5 mag, in the galaxy outskirts. The outermost loops (L2 and the new ones L6, L7, and L8) have bluer colors $0.5 \, \mathrm{mag} \leqslant g - r \leqslant 0.65$ mag than most of the galaxy bulk.

In the inner $3'$, the color map reveals the spiral-like system of dust lanes, more elongated toward the N–NE (see Figure 5). We catch two other "dust arms" that are more extended but less dense than the nuclear counterparts. On the NW region of the galaxy there are several blue patches with $g - r \leqslant 0.6$–0.7 mag. One of the most extended is the *plume*, as named by Schweizer (1980), which is about $2'$ ($\sim$12 kpc) long on the NW side. It has a very elongated shape, with the bluest colors concentrated in knots on the NW edge ($g - r \sim 0.6$ mag), while it appears in a more diffuse shape toward the SE. Close to the plume, on the north with respect to the galaxy center, we detect a blue tail, with similar colors to the plume (see Figure 5). Its shape and colors might suggest a possible connection between the two features.

On the south side of the nucleus, there are two peculiar features: the "ϕ-shape," first detected by Richtler et al. (2012), which is bluer ($g - r \sim 0.68$ mag) than the background galaxy light, and the "Y-shape" located at about $4'.6$ SW from the
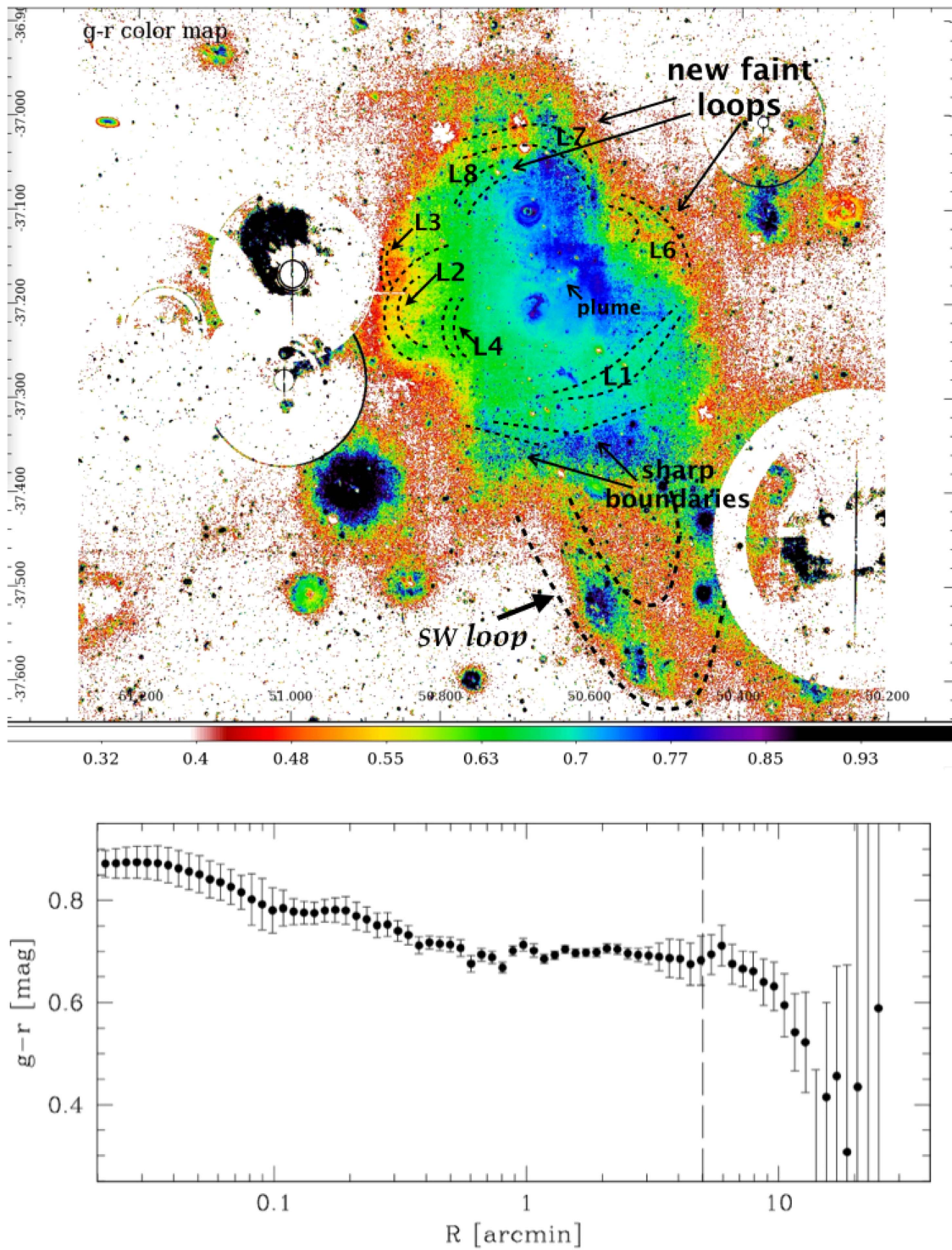
Figure 4. Top panel: $g − r$ color map in the same area shown in Figure 3, where the most luminous substructures are marked in the image. The $g − r$ levels are shown in the color bar. Bottom panel: azimuthally averaged $g − r$ color profiles for NGC 1316 as a function of the fitted ellipses' semimajor axis. The vertical long-dashed line indicates the transition radius at $R = 5\farcm5$, between the main galaxy body in NGC 1316, fitted by a Sérsic $n \sim 4$ law, and its outer exponential stellar halo (see Section 5.1 for details).

galaxy center, with redder colors (0.8 mag $\leqslant g − r \leqslant$ 1 mag) than the average adjacent regions, so it is probably patchy dust.

5. Isophote Analysis: Light Distribution of NGC 1316 Out to 200 kpc

On the full sky-subtracted mosaic, in each band, we extracted the azimuthally averaged intensity profile by using the IRAF task

ELLIPSE. All the bright sources (galaxies and stars) and background objects have been accurately masked. The fit is performed in elliptical annuli centered on NGC 1316, and the semimajor axis extends out to the edge of the mosaic. We derived the azimuthally averaged surface brightness profiles (see Figure 6), the position angle (P.A.) and ellipticity ($\epsilon = 1 − b/a$, where b/a is the axial ratio of the ellipses) profiles (see Figure 7), and the
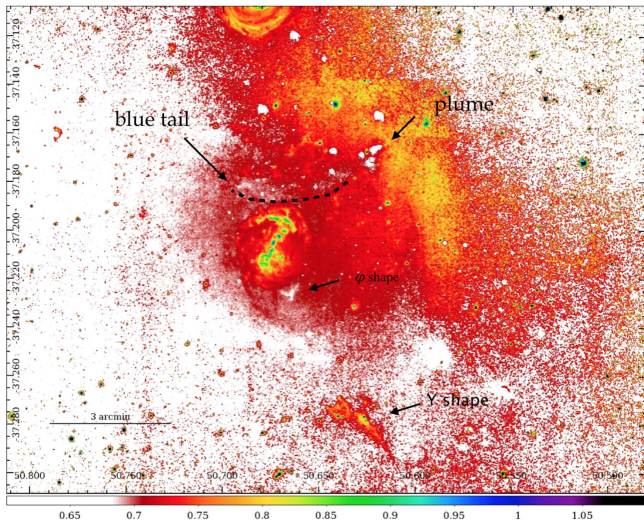
Figure 5. Zoom of the $g - r$ color map in the galaxy center from the image shown in Figure 4. North is up and east is on the left.

color $g - r$ profile (see Figure 4, bottom panel) as a function of the semimajor axis. From the intensity profiles in both g and r bands, shown in the left panel of Figure 6, we estimated the outermost radius $R_{\rm lim}$ from the center of the galaxy where the galaxy's light blends into the average background level, which is the residual after subtracting the sky frame, and therefore very close to zero (see Iodice et al. 2016). For both the g and r bands, we derived $R_{\rm lim} \simeq 33'$ ($\sim 200\,\mathrm{kpc}$). At this distance from the galaxy center, the surface brightness profiles reach to $\mu_g = 30 \pm 1\,\mathrm{mag\,arcsec}^{-2}$ and $\mu_r = 29 \pm 1\,\mathrm{mag\,arcsec}^{-2}$ (see Figure 6, right panel). The error estimates on the surface brightness magnitudes take the uncertainties on the photometric calibration (~ 0.001–0.002 mag) and sky subtraction (~ 0.02–0.03 counts) into account (Capaccioli et al. 2015; Iodice et al. 2016). The light profiles in g and r bands are three times more extended and about five times deeper than the light profile published by Caon et al. (1994) in the B band[21] (see right panel of Figure 6). Besides, the agreement between the surface brightness derived from the VST image in the r band and literature data is satisfactory at all radii.

Using the growth curve, we derived the total magnitudes and effective radii (R_e) inside $33'$ in the g and r bands. In the g band, $m_{\rm tot} = 8.43 \pm 0.003$ mag, and in the r band, $m_{\rm tot} = 7.713 \pm 0.002$ mag (see also Table 1). The absolute magnitudes and the total luminosity in solar units[22] in the g band are $M_g = -23.16$ mag and $L = 3.11 \times 10^{11} L_\odot$, respectively. The effective radii in the g and r bands are $R_e = 2.'22$ ($\sim 13\,\mathrm{kpc}$) and $R_e = 2.'23$, respectively. Therefore, the surface brightness profiles extend out to $\sim 15 R_e$. The average $g - r \sim 0.72$ mag, and, inside R_e, it is $g - r \sim 0.74$ mag.

Taking into account the average $g - r$ color and the age estimate of 2–3 Gyr, given by the color distribution of the GCs (Richtler et al. 2012), by using the stellar population synthesis model (Ricciardelli et al. 2012; Vazdekis et al. 2012), we estimate a stellar mass-to-light ratio (M/L) in the g band in the

range $1.67 \leqslant M/L \leqslant 2.66$. Therefore, the total stellar mass is in the range $5.2 \leqslant M \leqslant 8.3 \times 10^{11} M_\odot$.

The P.A. and ellipticity profiles are shown in Figure 7. For $R \geqslant 0.'01$, i.e., outside the central seeing region, the P.A. and ellipticity profiles in the g and r bands are consistent. For $R \leqslant 0.'1$, a strong twisting of about $40°$ and an increasing ellipticity from 0.2 to 0.4 are observed. For $0.1 \leqslant R \leqslant 4'$ (0.6–24 kpc), the P.A. is almost constant at $\sim 50°$–$55°$ and ellipticity shows a decline from 0.4 to 0.25. At larger radii, for $R \geqslant 5'$, an abrupt variation of about $30°$ is observed in P.A. while the ellipticity increases again to about 0.4.

5.1. Fit of the Light Profile

In order to define the scales of the main components dominating the light distribution in NGC 1316, we performed a multicomponent fit to reproduce the surface brightness profile, as done for the brightest cluster galaxies (BCGs) at the center of the groups and clusters (Seigar et al. 2007; Donzelli et al. 2011; Arnaboldi et al. 2012; Cooper et al. 2013, 2015a; Huang et al. 2013; Iodice et al. 2016; Rodriguez-Gomez et al. 2016). BCGs consist of at least two components, the bright spheroidal body and the outer and very extended, moderately flattened, stellar halo.

In Figure 8 (left panel) we compare the azimuthally averaged surface brightness profiles of NGC 1316 with those derived for NGC 1399 (Iodice et al. 2016), in the g and r bands. Overall, the light profiles are very similar. Inside $R \leqslant 10'$, NGC 1316 is brighter than NGC 1399. At larger radii, the flux levels and the exponential decline of the surface brightness profiles of both galaxies are comparable. Given that, according to Iodice et al. (2016), we used the superposition of a Sérsic law plus an exponential function to fit the light profile of NGC 1316.[23]

We performed a least-squares weighted fit[24] of the azimuthally averaged surface brightness profile in the r band, which is less perturbed by dust absorption in the center, for $R \geqslant 0.'02$, to exclude the central seeing-dominated regions. The structural parameters and the $\tilde{\chi}^2$ values are listed in Table 2. Results are shown in the right panel of Figure 8. We found that inside $R \leqslant 5.'5$ the Sérsic law coincides with a de Vaucouleurs law, since $n \sim 4$. This component accounts for the inner and most luminous part of the galaxy, the *central spheroid*. For $R \geqslant 5.'5$, the light profile is well reproduced by the exponential function. The total magnitude obtained from the fit is ~ 0.5 mag brighter than that measured from the growth curve. Such a difference is due to the exclusion of the central seeing-dominated regions ($R \leqslant 0.'02$) from the fit.

The above analysis allows us to conclude that there are two main components dominating the light distribution in NGC 1316 and to estimate the *transition radius* between them

---

[21] Following the color transformation by Fukugita et al. (1996), $B - r = 1.33$, the B-band profile is shifted to the r.

[22] We used $m_g = 5.45$ mag and $m_r = 4.76$ mag for the solar magnitudes in g and r bands, respectively, given at the following Web site: http://www.ucolick.org/~cnaw/Sun.html.

[23] The Sérsic law is given by the equation $\mu(R) = \mu_e + k(n)\left[\left(\frac{R}{r_e}\right)^{1/n} - 1\right]$, where R is the galactocentric distance, r_e and μ_e are the effective radius and effective surface brightness, respectively, and $k(n) = 2.17n - 0.355$. The exponential law is given by $\mu(R) = \mu_0 + 1.086 \times R/r_h$, where μ_0 and r_h are the central surface brightness and scale length, respectively (Iodice et al. 2016).

[24] To perform the least-squares weighted fit, we used the MINUIT package (James & Roos 1975), which is a physics analysis tool for function minimization and error analysis distributed by CERN (see https://www.cern.ch/minuit). As a user-defined function we adopted the *chi-square*, defined as $\chi^2(\alpha) = \sum \frac{[f(x_i, \alpha) - e_i]^2}{\sigma_i^2}$, where α is the vector of free parameters being fitted, and the σ_i are the uncertainties in the individual measurements e_i. We computed the reduced chi-square $\tilde{\chi}^2 = \chi^2/N$, where N is the number of measured values. The best is given when $\tilde{\chi}^2 \sim 1$.
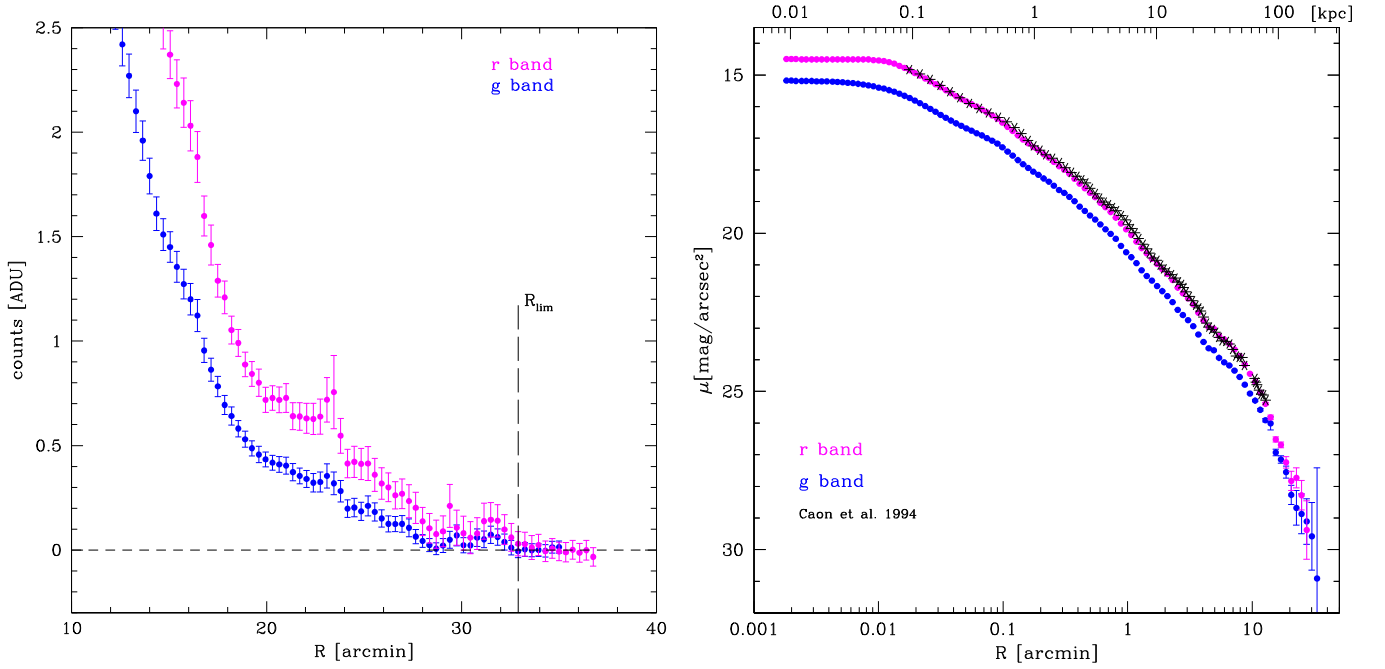
Figure 6. Left panel: intensity profiles of NGC 1316 in the *g* (blue points) and *r* (magenta points) bands out to the regions of the background level (short-dashed black line). The outer radius from the galaxy center where the galaxy's light blends into the background level is at $R_{lim} \simeq 33'$ (long-dashed line). Right panel: azimuthally averaged surface brightness profiles of NGC 1316 in the *g* and *r* bands derived from VST mosaics, compared with literature data from Caon et al. (1994) (black asterisks), which are obtained by averaging the light profiles obtained along the major and minor axes of the galaxy.
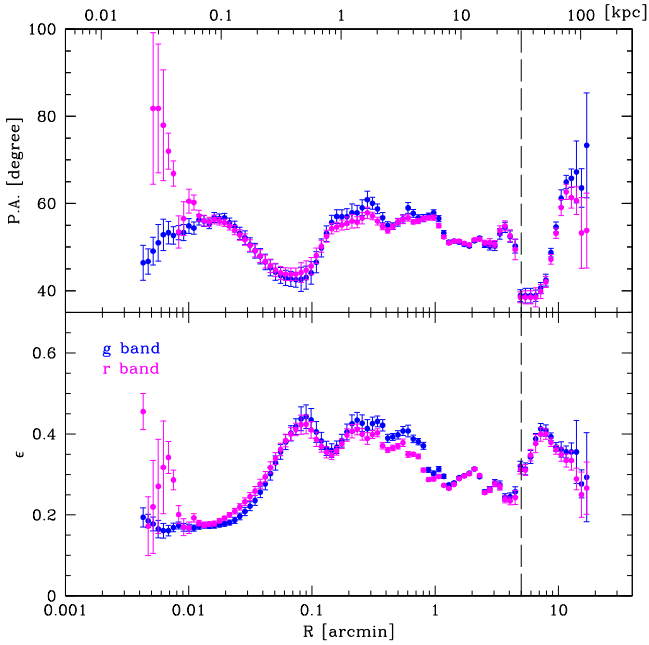

Figure 7. Ellipticity (bottom panel) and P.A. (top panel) profiles for NGC 1316 derived by fitting the isophotes in the *g*-band (blue circles) and *r*-band (magenta circles) images. The vertical long-dashed line indicates the transition radii at $R = 5'$, between the main galaxy body, fitted by a Sérsic $n \sim 4$ law, and the outer stellar exponential halo (see Section 5.1 for details).

at $R = 5'.5$. The presence of the two components is also consistent with the variations measured in the isophotes' ellipticity (ϵ) and P.A. profiles, in correspondence with $R = 5'.5$, where for $R \geqslant 5'.5$, ϵ increases from 0.22 to 0.4, and the P.A. shows a twisting by about 30° SE (see Figure 7). The central spheroid is redder ($g - r \sim 0.7$ mag) than the

envelope, which shows a gradient toward bluer colors from $g - r \sim 0.7$ mag at $R = 5'.5$ down to $g - r \sim 0.4$ mag at $R = 20'$ (see bottom panel of Figure 4).

As for NGC 1399, the outer exponential component represents physically the *stellar envelope*, which has a central surface brightness $\mu_0 = 22.79 \pm 0.10$ mag arcsec^{-2} and a scale length $r_h = 317 \pm 17''$ (~ 32 kpc) in the *r* band. These values are comparable with those estimated for the stellar exponential envelope of NGC 1399 (Iodice et al. 2016), which are $\mu_0 = 22.6 \pm 0.1$ mag arcsec^{-2} and $r_h = 292 \pm 4''$ (~ 28 kpc) in the *r* band. The fraction of the stellar envelope in NGC 1316 with respect to the total luminosity is ~ 0.36, which is almost half of the 60% estimated in NGC 1399 (Iodice et al. 2016).

6. Behind the Light: Loops, Ripples, and Accretion Remnants inside NGC 1316

From the isophote fit performed in the *r* band (see Section 5), which is less perturbed by dust in the central regions than the *g* band, we built a two-dimensional (2D) model of the light distribution, by using the BMODEL task in IRAF. We derived the residual map as the ratio between the image of the galaxy and its 2D model. The result is shown in Figure 9 (top panel), where we marked the most luminous ripples and loops already described in Section 4.1.

Morphology: Blended into the galaxy's light, in addition to the old and new substructures known for NGC 1316 (see Section 4.1), the VST *r*-band residual image reveals (i) a new and faint "bridge" connecting L1 with L4 and (ii) on the west side, two shell-like features protruding from the south part of the plume (see Figure 10). In projection, the inner shell is at about $2'.7$ from the center, while the outer one is at about $3'.5$. They are very red, with average colors $g - r \sim 0.8$ mag similar to those measured in the galaxy center (see Figure 4).
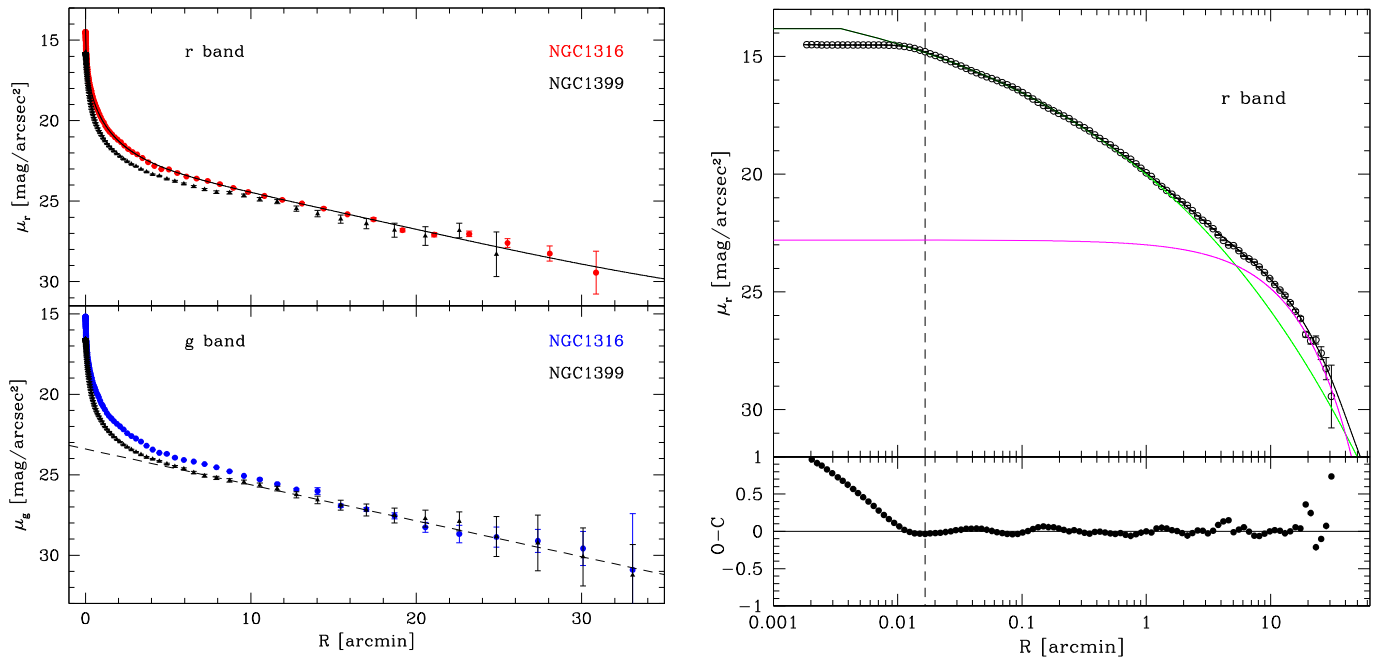
Figure 8. Left panel: azimuthally averaged surface brightness profiles of NGC 1316 in the g (bottom) and r (top) bands derived from VST mosaic, in linear scale, compared with those derived for NGC 1399 (black asterisks) from Iodice et al. (2016). The solid line is the resulting fit to the r-band profile. The dashed line is the exponential law adopted to fit the stellar halo in the g-band profile of NGC 1399 (see Iodice et al. 2016). Right panel: in the upper box are the azimuthally averaged surface brightness profile of NGC 1316 in the r band (open circles) and the resulting best fit obtained with a Sérsic law (green line) and an exponential law (magenta line) to match the outer stellar halo (blue line). The black solid line is the sum of the three components. The vertical dashed line delimits the region affected by the seeing, which is excluded from the fit. In the bottom box are plotted the residuals of the fit (observed minus fitted surface brightnesses).

Moreover, the residual image brings to light the impressive coherent spiral-like pattern of ripples up to the center of the galaxy and, on the SW at about 1.6 from the center, the bright overdensity region, labeled "O1" by Richtler et al. (2014). This is populated by several compact sources (see Figure 10), which might be star clusters. Richtler et al. (2014) suggested that, similarly to the plume, it could be another remnant of a dwarf galaxy.

The bright ripples R1 and R2, the plume, and the shells are features inside the transition radius $R = 5.5$ (see Section 5.1); therefore, they are part of the inner spheroidal component of the galaxy. All the loops from L1 to L9 contribute to the light of the outer stellar envelope.

Integrated colors: We derived the integrated $g − r$ colors in several loops, ripples, and substructures (i.e., the plume). The main aim is to compare them with the average value of the whole galaxy ($g − r = 0.717 \pm 0.005$ mag; see Table 1): this analysis helps to determine their origin. Regions were selected on the residual map, and polygons were defined covering the L1, L2, L3, and L4 (including the new faint bridge toward L1) loops, the plume region, ripples R1 and R2 (which includes the bright part close to the center), the two new faint loops L6 and L7 on the NW of NGC 1316 (see details in Figure 9), and loop L5 in the south. Results are shown in the bottom panel of Figure 9 and in Table 3.

By analyzing them, we conclude that (i) loops L1 and L4 seem to be a single structure, since they have similar colors ($g − r \simeq 0.63$–0.65 mag) and a faint bridge is detected between them (see the blue dashed lines in Figure 9); (ii) regions III and IV covering the new two faint loops L6 and L7 have similar colors ($g − r \simeq 0.58$ mag), and thus they could be the brightest part of a single giant loop in the galaxy

envelope, connecting also two other faint features on the south and on the north (see the blue dashed lines in Figure 9), with a diameter $\geqslant 10'$; and (iii) loops L2 and L3, being about 0.13 mag bluer than the average color of NGC 1316, could have an external origin, while the giant SW loop L5, which has comparable colors to those of the inner regions, could be coeval with the galaxy.

7. Discussion: Tracing the Buildup History of Fornax A

The deep and extended photometry of the VST mosaics allow us (i) to trace with great detail the morphology and structure of NGC 1316 out to $33'$ (~ 200 kpc $\sim 15 R_e$) from the galaxy center and down to $\mu_g \sim 31$ mag arcsec^{-2} and $\mu_r \sim 29$ mag arcsec^{-2}, (ii) to estimate the scales of the main components dominating the light distribution, and (iii) to give some constraints on the origin of the substructures found in each component by deriving the integrated colors. The main results are listed below.

1. New faint loops are discovered on the N–NW side of the galaxy envelope (we named them L6, L7, L8, and L9), in the range of surface brightness $29 \leqslant \mu_r \leqslant 30$ mag arcsec^{-2} (see Figures 2 and 3), and the giant ($\sim 0°.44 \sim 160$ kpc) L5 loop ($\mu_g \sim 29$–30 mag arcsec^{-2}) in the SW region is confirmed. The VST mosaic unveils the whole structure of L5: close to the galaxy it has a filament-like structure, while several bright blobs dominate the emission on the SE part of it. On the opposite side to L5, with respect to the galaxy center, the new outer loop L9 on the NW is fainter and less extended than L5. It appears as a very curved arc with a radius of about $15'$ (~ 91 kpc). Inside the main body, the deep VST images reveal that loops L1 and L4 are part of

Table 2
Structural Parameters Derived from the Multicomponent Fit of the Surface Brightness Profile in the r Band for NGC 1316

μ_e (mag arcsec^{-2})	r_e (arcsec)	n	μ_0 (mag arcsec^{-2})	r_h (arcsec)	$m_{\rm tot}^{\rm ser}$ (mag)	$m_{\rm tot}^{\rm exp}$ (mag)	$m_{\rm tot}$ (mag)	$\tilde{\chi}^2$
(1)	(2)	(3)	(4)	(5)	(6)	(7)	(8)	(9)
20.76 ± 0.05	87 ± 2	4.49 ± 0.05	22.79 ± 0.10	317 ± 17	7.67	8.29	7.18	1.035

Note. Columns (1)–(5): structural parameters characterizing the empirical laws adopted to fit the surface brightness profile. The effective surface brightness μ_e and the central surface brightness μ_0 are in mag arcsec^{-2}. The effective radius r_e and the scale length r_h are in arcsec. $m_{\rm tot}$ is the total magnitude of each component. Columns (6)–(8): total magnitudes for each component (columns (6) and (7)) and total magnitude of the fitted profile (column (8)). Column (9): reduced $\tilde{\chi}^2$. The confidence level of each least-squares fit is about 50%.

a unique and more extended structure; they seem to be connected by a faint bridge (see Figure 9).

2. By fitting the azimuthally averaged surface brightness profile in the r band, we identify two distinct components in NGC 1316. Inside $R \leqslant 5'.5$ (~ 33 kpc), i.e., for $R \leqslant 2.5 R_e$, the main body of the galaxy has a dominant $\sim r^{1/4}$ spheroidal component (see Section 6). For $R \geqslant 5'.5$, we map the outer envelope out to about 200 kpc from the galaxy center. It has an exponential decline (see Figure 8) and a steep gradient toward bluer colors with respect to the central spheroid (see Figure 4). The presence of the two components is also consistent with the variations measured in the isophotes' ellipticity and P.A. profiles, in correspondence with the transition radius given above (see Figure 7).

3. Loops L1, L2, L3, L4, and the new ones L6 and L7 are inside the stellar envelope. They are bluer than those in the central spheroid (see Figures 2, 4, and 9). The bluest ones are L2 and L3, on the east side, with $g - r \sim 0.54$ mag. The new loops L6 to L8, located on the N–NW side of the envelope, have comparable colors, $g - r = 0.58$ mag, suggesting that they could be the brightest part of a single giant loop. The giant SW loop L5, even if it is in the region of the envelope, has similar colors to those of the regions of the galaxy, which is $g - r \sim 0.65$ mag (see Figure 9).

The analysis of the integrated colors for the different structures in the central spheroid and outer envelope suggests that (i) the giant loop L5 could be "coeval" with the central spheroid, since they have comparable colors, and thus it can be considered as a tidal tail of material expelled from the galaxy during a merging event in its formation history; (ii) the plume and the extended tail detected SE to it (see Figure 5) are the bluest features inside the central spheroid, and therefore it is reasonable to assume that this structure was not formed together with the host galaxy, but it could be the remnant of a smaller infalling galaxy; and (iii) the bluest loops detected in the galaxy envelope could be the sign of the minor accretion events that are contributing to the mass assembly of this component. Therefore, based on the above results, the main conclusion of this work is that for NGC 1316 we are still observing the relics (i.e., loop L5 and L9) of the first main process that formed the central spheroid, and we are catching in the act the second phase of the mass assembly (Cooper et al. 2010; Oser et al. 2010), where the accretion of smaller satellites is ongoing and it is building up the galaxy outskirts.

In the following subsections we discuss in detail the main formation processes that could have formed the central spheroid and the envelope by comparing the observed properties with the theoretical predictions.

7.1. How Did the Central Spheroid Form?

To date, from the extensive literature available for NGC 1316 (see Section 2), there are two processes proposed for the formation of this galaxy: the major merging of two disk galaxies and the minor merging of a giant early-type disk galaxy with a lower-mass late-type galaxy.

Numerical simulations of a major disk–disk merger show that during the final phase of such a merger, the violent relaxation transforms the stellar content of the two disks into a spheroidal remnant having an $r^{1/4}$ density distribution (Barnes 1992; Hernquist & Spergel 1992; Mihos & Hernquist 1996). This would be consistent with the surface brightness distribution observed for NGC 1316 (see Section 5.1). Besides, the presence of shells or tidal tails also detected in this galaxy can be considered a "sign" of the past merging in the remnant object.

Alternatively, the shells and ripples, as well as the nuclear dust, clearly detected in NGC 1316, could have formed throughout the accretion of one or more smaller companion galaxies (e.g., Quinn 1984) by an early-type disk galaxy. According to the theoretical predictions, this formation process can work in forming tails with different length and surface brightness (Balcells 1997), as observed in NGC 1316, which are the SW loop L5 and the fainter and less extended loop L9 on the NW (see Figure 3). If the accreted galaxy is massive enough, the giant loop L5 could be the returning material during the merging (e.g., Hernquist & Spergel 1992). Taking into account that both loops are void of ionized gas (Schweizer 1980; Mackie & Fabbiano 1998), the brightest and reddest knots inside loop L5 (see Figures 3 and 4) are not star-forming regions, but more reasonably they could be remnant debris.

Based also on the main conclusion of this work, we suggest that the formation history of NGC 1316 is even more complex than those described above: after the main process that formed the central spheroid, many other accretion events are going on, which are building up the galaxy outskirts and are perturbing the inner structure. Therefore, in order to reproduce all the observed properties of NGC 1316 (i.e., morphology, gas content, kinematics), one needs a set of simulations of the interacting/merging galaxies, spanning a wide range of masses and morphological types, which include the secondary infall of small satellite galaxies. This is beyond the scope of the present paper. However, as a starting point for a future work, we investigate how the main properties of the merger remnant formed by the two "simple" cases proposed above compare with the observations. To this aim, we used the
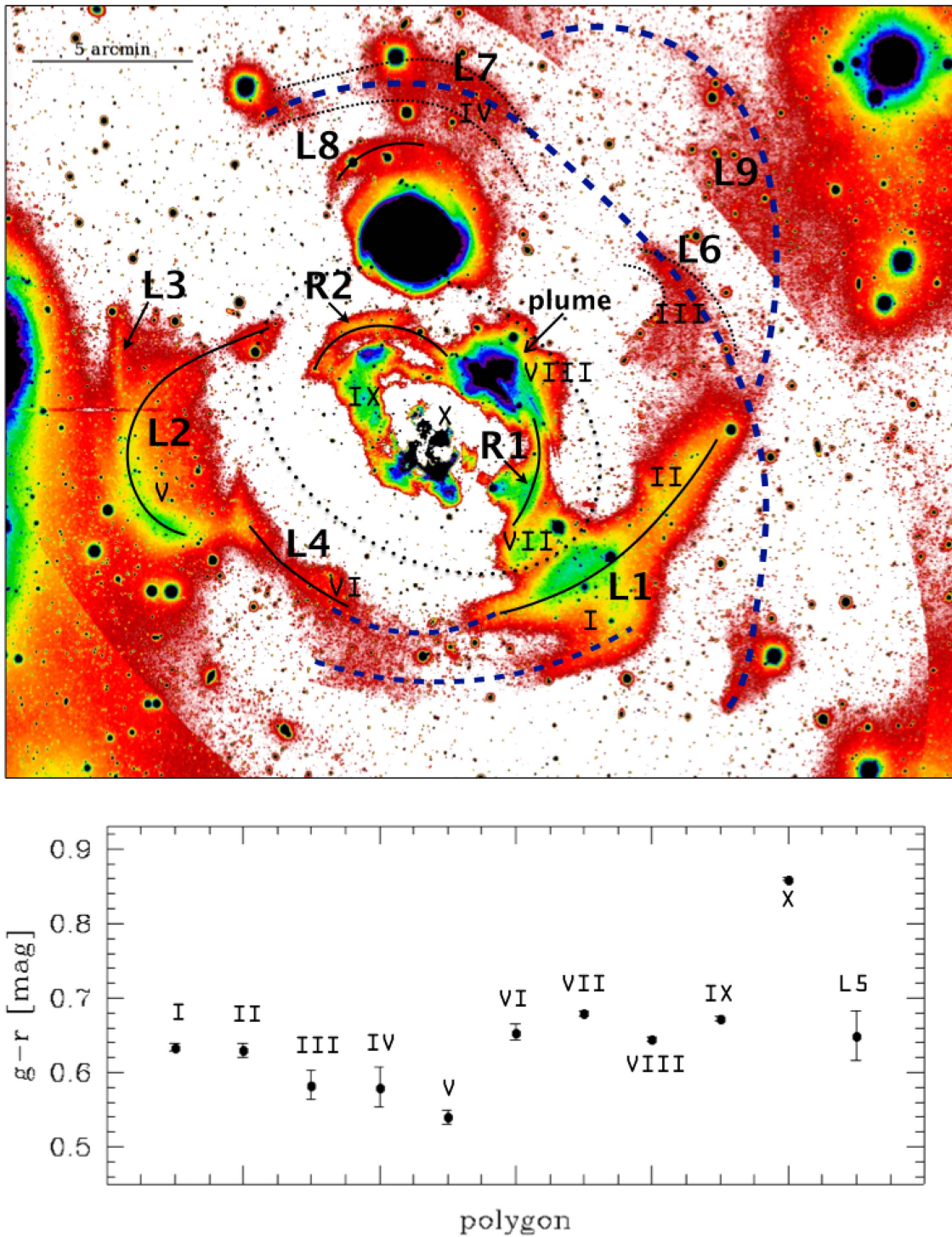
Figure 9. Top panel: residual map obtained by the ratio of the image and the two-dimensional model in the *r* band. The image size is ~29.2 × 23.'3. The most luminous substructures are marked in the image. The known loops presented by Schweizer (1980) and Richtler et al. (2014) are L1, L2, L3, and L4. The blue dashed lines trace the new and faintest features found in the deep VST data (see also Figure 3). Numbers from I to X indicate the regions where we computed the integrated $g - r$ colors shown in the bottom panel. The dotted ellipses correspond to the isophote at the transition radius $R = 5'$ (see Section 5.1 for details). Bottom panel: integrated $g - r$ colors in the 10 regions marked on the residual map (from I to X) and that are computed for the SW loop L5.

GalMer simulations database (Chilingarian et al. 2010). By looking at the remnants from all possible combinations of merging, with different mass ratio and morphological types, we extracted from the GalMer database the remnant at ~3 Gyr, which is the upper limit age estimated for the last merger event (Goudfrooij et al. 2001; Richtler et al. 2014),

that matches with the observed properties in NGC 1316. In particular, we check for the overall morphology, including the presence of shells/ripples/tails, the surface brightness profile, the internal kinematics of stars, and the amount of gas (see Section 2). Results are discussed in the following section.
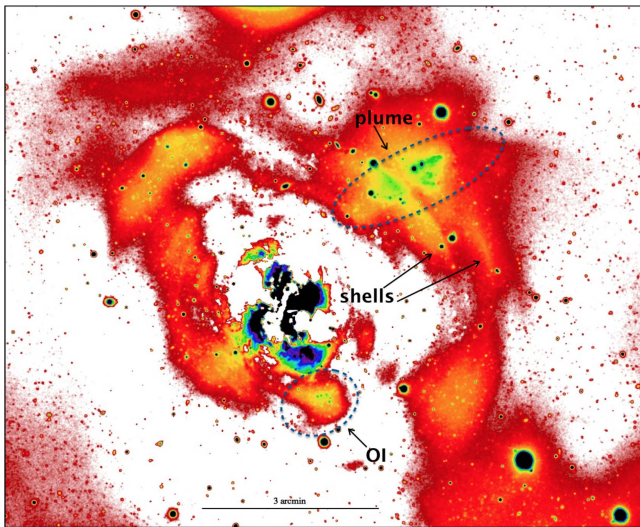
Figure 10. Zoom-in of the central regions of the residual map shown in Figure 9. The image size is $10.85 \times 8'.9$. The plume and the "OI" substructures are encircled by the blue dashed line.

Table 3
Integrated Magnitude in the g Band and $g - r$ Color Derived in the Polygons Covering the Substructures Shown in Figure 9

Region	Structure	m_g (mag)	$g - r$ (mag)
(1)	(2)	(3)	(4)
I	L1	12.328 ± 0.004	0.634 ± 0.006
II	L1	13.53 ± 0.01	0.63 ± 0.01
III	L6	14.48 ± 0.01	0.58 ± 0.02
IV	L7	15.51 ± 0.02	0.58 ± 0.03
V	L2	12.318 ± 0.008	0.54 ± 0.01
VI	L4	13.346 ± 0.009	0.65 ± 0.01
VII	R1	12.351 ± 0.003	0.679 ± 0.005
VIII	plume	11.763 ± 0.003	0.645 ± 0.004
IX		11.096 ± 0.002	0.672 ± 0.004
X	center	11.906 ± 0.002	0.860 ± 0.003
	L5	12.88 ± 0.02	0.65 ± 0.03

Note. Columns (1) and (2): number identifying the regions and features shown in Figure 9. Column (3): integrated magnitude in the g band. Column (4): integrated colors. Values were corrected for the Galactic extinction by using the absorption coefficients $A_g = 0.069$ and $A_r = 0.048$ derived according to Schlegel et al. (1998).

7.1.1. Tests on the Formation Scenarios for NGC 1316: Disk–Disk Merging versus Tidal Accretion

In Figures 11 and 12 we show the results from the GalMer database[25] for a major merging of two disks and for a minor merging of a preexisting giant S0 galaxy with a dwarf late-type disk, respectively. We show the density distribution of stars plus gas (top left panels), the distribution of gas (top right panels), and the 2D map of the stellar kinematics, i.e., rotation

---

[25] From the GalMer database at http://galmer.obspm.fr/ the selected simulations have the following orbital parameters. Major merging: mass ratio = 1:1; spin = prograde; inclination = 45°; initial distance = 100 kpc; pericentral distance = 8 kpc; motion energy = 2.5. The snapshot is extracted at the time of 3 Gyr. The angles of the viewport are $\phi = 68°$ and $\theta = -31°$. Minor merging: mass ratio = 10:1; spin = prograde; inclination = 33°; initial distance = 100 kpc; pericentral distance = 8 kpc; motion energy = 2.5. The snapshot is extracted at the time of 2.5 Gyr. The angles of the viewport are $\phi = -96°$ and $\theta = -51°$.

velocity and velocity dispersion (middle panels). The above maps allow us to qualitatively describe the main expected structural properties of the remnants, such as the presence of tidal features, the total mass and luminosity, surface brightness profiles, and isophote shape. They are listed in Table 4, which includes also those observed in NGC 1316. In the following we discuss how observations and models compare.

Morphology: A spheroidal remnant galaxy with shells and extended tidal loop on the south, plus other faint tails in the outskirts (see left-top panel of Figure 11), is obtained by an equal-mass merging of two giant spiral galaxies, with a total stellar mass of $\sim 10^{10} M_\odot$ and a fraction of gas of about 0.1. In the adopted projection on the sky of the remnant, the south tidal loop extends out to about 190 kpc and has several bright knots. The NW tidal tail is less luminous than the southern one. For both features, from the density map shown in the top left panels of Figure 11, we derived the density ratio between the mass of the tails and the mass in the center: it is about 10^{-3}–10^{-5}. In NGC 1316 the south tidal loop has a radius of about 160 kpc, and it is characterized by several bright knots (see Figure 2); thus, it is similar in shape and extension to that in the simulated merger remnant. Taking into account that the surface brightness of the south loop is in the range $29 \leqslant \mu_r \leqslant 30$ mag arcsec^{-2} (see Figure 3), this corresponds to $\sim 10^{-5}$ fainter than the galaxy center. Such a value is therefore comparable with that estimated in the merger remnant.

The minor merging of a preexisting S0 galaxy with a dwarf late-type disk (mass ratio 10:1) also generates a spheroidal remnant galaxy, which has a very perturbed morphology by ripples and outer faint tails (see top left panel of Figure 12). Differently from the previous model, there are no prominent loops in the galaxy outskirts.

Gas content: In the selected remnants, gas is concentrated at small radii, with some other fainter emissions associated with the outer tails (see the top right panel of Figure 11). In both remnants, the ratio between the density of stars and that of the gas in the center is about 10^{-3}–10^{-4}, which is consistent with a ratio of about 10^{-4} observed in NGC 1316. Differently from what is observed in NGC 1316, gas is also detected in the outer tails formed in the disk–disk major merging. The absence of prominent star-forming tidal tails and the lack of H I in them (Horellou et al. 2001) suggest that NGC 1316 would be an evolved disk–disk merger remnant.

Surface brightness and isophote shape: By performing an ellipse fitting of the isophote in both remnants, we found that, as observed in NGC 1316 (see Section 6), the azimuthally averaged surface brightness profile of the main body follows an $r^{1/4}$ behavior, with several bumps at larger radii that are the sign of shells and tails (see the bottom panels of Figures 11 and 12). For the minor merger remnant, the surface brightness profile shows a change in the slope at larger radii, which reflects the existence of a second component. In both models the isophotes have an ellipticity (0.3–0.4) and twisting comparable to those found in NGC 1316 (see Figure 7). For the major merging remnant, the ellipticity increases with distance from the galaxy center (from 0.1 to 0.4), while in the minor merging remnant it remains almost constant at about 0.3, more similar to what is observed in NGC 1316.

Kinematics: The stars in both remnants have a significant rotation with $V_{max} \sim$ 120–130 km s^{-1} and quite large velocity dispersion in the center ($\sigma_c \sim$ 160–180 km s^{-1}; see Table 4). The V_{max}/σ_c is about 0.67 in the major merging remnant, which
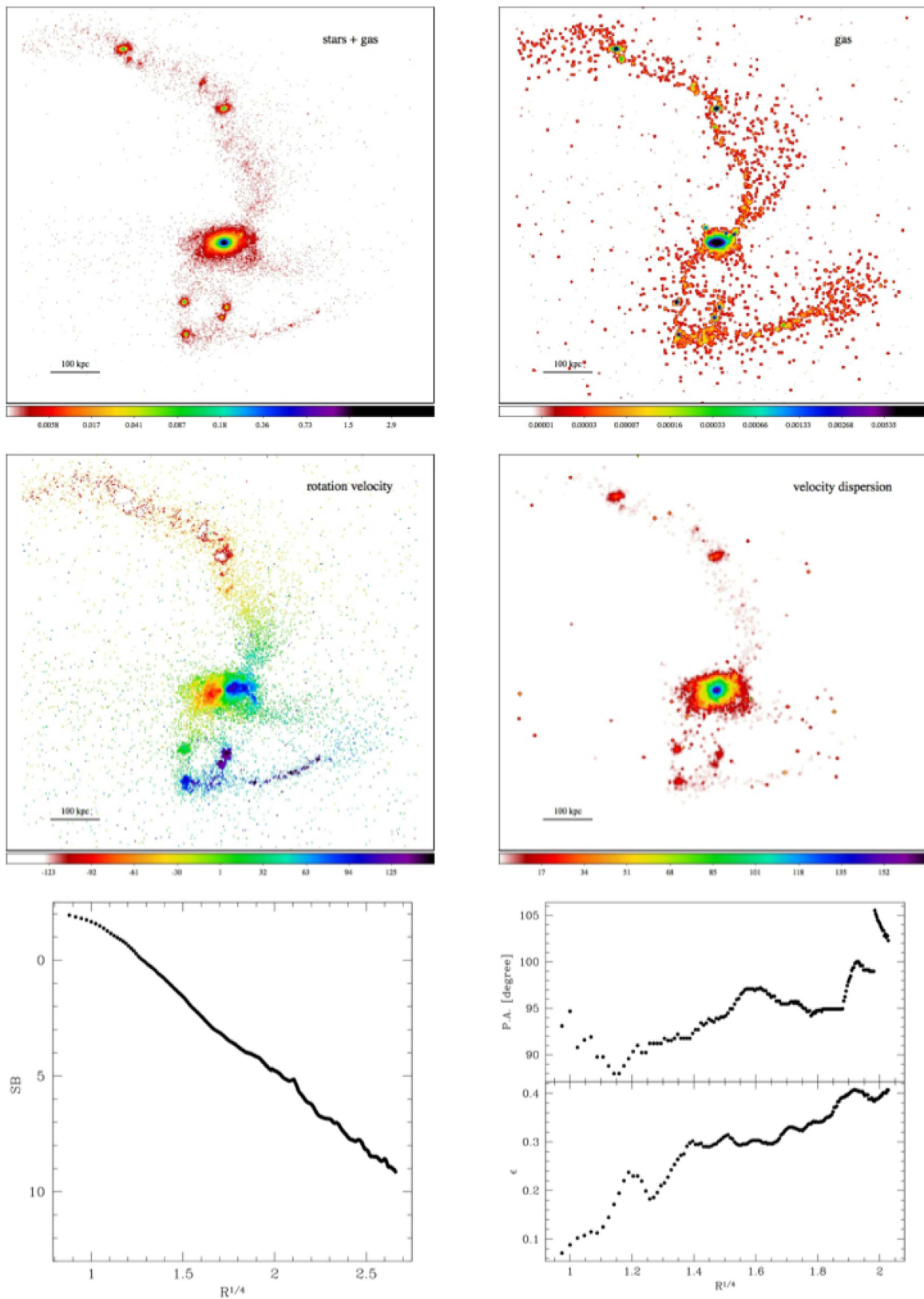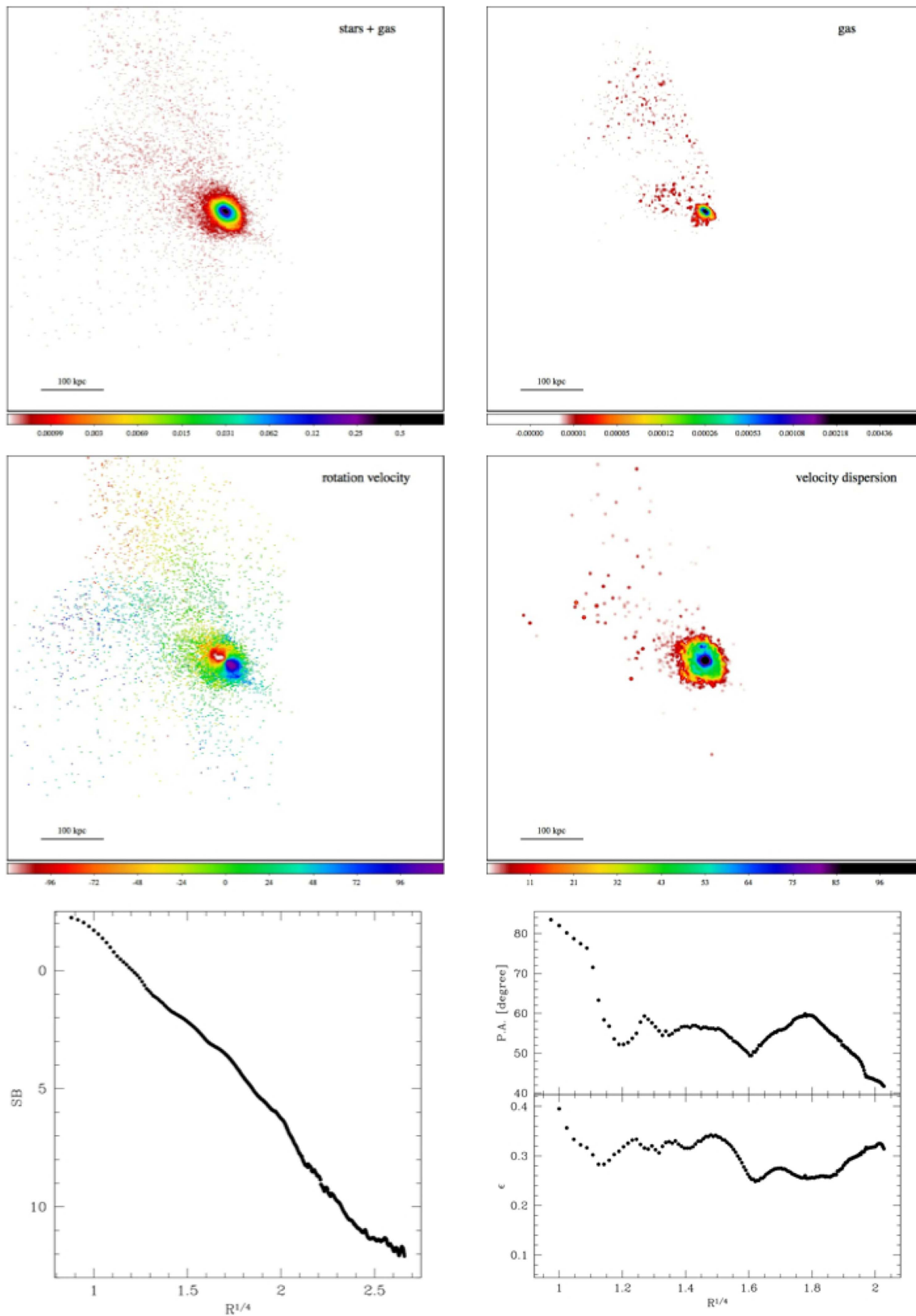
Figure 11. Extracted snapshot at 3 Gyr from the GalMer database for a merging of two giant equal-mass disk galaxies. The total (stars + gas) surface density and the gas surface density are shown in the top left and top right panels, respectively. The stellar kinematics is shown in the middle panels (rotation velocity on the left and velocity dispersion on the right). The bottom panels show the azimuthally averaged surface brightness profile (left) and the P.A. and ellipticity profiles (right) of the fitted isophotes.

is more similar to the value of ∼0.6 observed in NGC 1316. The remnant by the other proposed scenario has a bit larger V_{max}/σ_c ratio (∼0.75). The main difference is in the velocity dispersion at larger radii, since for NGC 1316 it remains at higher levels (∼150 km s^{-1} at $3R_e$; see Table 4) than in the simulations. As we pointed out before, in NGC 1316 several

14

Figure 12. Extracted snapshot at 3 Gyr from the GalMer database for a merging of two giant equal-mass disk galaxies. The total (stars + gas) surface density and the gas surface density are shown in the top left and top right panels, respectively. The stellar kinematics is shown in the middle panels (rotation velocity on the left and velocity dispersion on the right). The bottom panels show the azimuthally averaged surface brightness profile (left) and the P.A. and ellipticity profiles (right) of the fitted isophotes.

secondary accretion events are contributing to the mass assembly; thus, they could be responsible for the increasing velocity dispersion.

In summary, the above analysis shows that the main difference between the two scenarios is the presence of the outer tails, observed in NGC 1316, which are expected for a

Table 4
Main Parameters of the Remnants Derived by the GalMer Simulation, Compared with Those Observed in NGC 1316

Model	$M_{\rm ratio}$	Morphology	Gas/Star	SB Profile	ϵ	$V_{\rm rot}^{\rm max}$ (km s^{-1})	σ_c (km s^{-1})	$\sigma[3R_e]$ (km s^{-1})	$M_{\rm tot}$ $10^{11}\,M_\odot$
(1)	(2)	(3)	(4)	(5)	(6)	(7)	(8)	(9)	(10)
Sa+Sa	1	loops $R \sim 190$ kpc	10^{-3}–10^{-4}	$r^{1/4}$	0.1–0.4	120–130	180	91	2
S0+dSa	10	no loops	10^{-3}–10^{-4}	$r^{1/4} +$ exp	$\sim$0.3	120–130	160	70	1.3
NGC 1316		loops $R \sim 165$ kpc	10^{-4}	$r^{1/4} +$ exp	$\sim$0.3	150–170	250	150	5.2–8.3

Note. Column (1): GalMer simulations. Sa+Sa indicates the major merging of two equal-mass spiral galaxies; S0+dSa is the merging of a giant S0 galaxy with a dwarf late-type galaxy, which is 10 times less massive than the S0. Column (2): mass ratio of the merging galaxies. Column (3): features observed in the remnant like tails and loops. Column (4): mass ratio between the gas amount and mass of the stars. Column (5): shape of the azimuthally averaged surface brightness profile (SB). Column (6): ellipticity of the isophotes. Column (7): maximum rotation velocity of the stars. Columns (8) and (9): central velocity dispersion of the stars and its estimate at R_e, respectively. Column (10): total stellar mass. In the last line of the table are listed all the above quantities observed for NGC 1316.

major disk–disk merger but not so much for the unequal-mass merger. Therefore, taking also into account that the $V_{\rm max}/\sigma_c$ ratio is more similar to the value observed in NGC 1316 (see Table 4), the disk–disk major merging might be slightly favored. In contrast to this, the extension, gas content, and surface density of the outer tails do not fit with those observed in NGC 1316. In the model, the outer tails have comparable extensions and density (see Figure 11). In NGC 1316 the NW loop L9 is less extended and fainter than the SW loop L5 (see Figure 3). Also the gas content is different: in the tidal tails resulting from the disk–disk merging, the H I gas is detected along the whole extension of both tails, while the minor merging of an S0 with a dwarf late-type disk has a very small amount of neutral gas in the outer faint tails. In NGC 1316, there is no detection of neutral atomic gas in correspondence with the two giant outer loops L5 and L9, while emission is detected in four clumps in the galaxy outskirts (see Section 2).

As a conclusive remark, a more complex simulation is therefore needed to account for the structure and kinematics of NGC 1316. In particular, by studying the faint galaxy outskirts, one key point is that the structure and stellar population of the outer tails, which have different extensions, are devoid of gas and star-forming regions and have comparable colors to the main body. These characteristics would exclude the major disk–disk merging as a formation process for NGC 1316. The unequal-mass merging of an early-type disk with a companion galaxy remains a probable scenario to account for the formation of NGC 1316. It also reconciles with results by dynamical models made for NGC 1316, which suggested that the dark matter halo shows a central density comparable to those of massive elliptical galaxies (McNeil-Moylan et al. 2012; Richtler et al. 2014), rather than of spiral galaxies. But it needs further investigation. One case to be verified is the interaction of a giant S0 galaxy with an intermediate late-type galaxy, to check whether this process might give different results about the structure of the tidal tails. This option is not available in the GalMer database.

7.2. The Buildup of the Stellar Halo in NGC 1316

In this section we attempt to trace the buildup history of the stellar halo of NGC 1316 by comparing the observed properties with the theoretical predictions.

Cosmological simulations of galactic stellar halo formation by the tidal disruption of accreted material are able to give a complete set of "observables," such as structure, density profiles, and metallicity, that can be compared with real data. Cooper et al. (2010) made a detailed analysis of the properties for six simulated stellar halos. They found that the assembly history is made either by a gradual accretion of several progenitors with roughly equal mass or by the accretion of one or two systems. The resulting morphology of the stellar halo is different in the two cases (see Figure 6 in Cooper et al. 2010). The stellar halos built up by the gradual accretion are the most extended, out to 70–100 kpc, and have several streams, shells, and other irregular structures, which are more evident at larger radii. On the contrary, the accretion of one or two massive satellites generates smaller stellar halos with a strong central concentration. All features span a surface brightness range of 24–35 mag arcsec^{-2} in the V band. The brightest and most coherent structures detectable in the stellar halo come from the most recent accretion events. Also the shape of the density profiles changes between the halos formed by many progenitors and those formed by a few progenitors, with the former being steeper and well fitted by a Sérsic profile with $n \sim 1$. Halos with several dominant progenitors show an almost flat metallicity profile, out to the outermost radii, while stronger metallicity variations are observed in the case of a small number of accreted satellites.

The deep VST photometry allows us to map the faint regions of the stellar envelope of NGC 1316 out to 33$'$ ($\sim$200 kpc). This component starts to dominate the light for $R \geqslant 5\!'.5$ ($\sim$33 kpc) and has a surface brightness in the range of 26–30 mag arcsec^{-2} (see Section 5.1). Therefore, at these large distances and surface brightness levels we are able to make a direct comparison between the observed properties and those from theoretical predictions described above.

The stellar envelope in NGC 1316 is characterized by several discrete and luminous substructures: the south extension of the loop L1, the whole bright part of loops L2 and L3, and all the new fainter loops L6, L7, and L8 detected in the VST images (see Figure 9, top panel). All of them have bluer $g - r$ colors than the substructures in the inner spheroid (see Figure 9, bottom panel). At larger radii (for $R \geqslant 20'$), the light in the stellar envelope appears to be in a more diffuse form, which is probably mixed with the unbound component of the intracluster light. Probably, many other fainter loops are still present, but their luminosities are below our detection limit. Compared to the simulated halos presented by Cooper et al. (2010), the stellar halo in NGC 1316 has very similar

morphology, surface brightness levels, and light distribution to those of the Aq-C model (shown in Figure 6 of that paper), even if the simulated galaxy is about one order of magnitude less massive than NGC 1316. The Aq-C model is characterized by several loops in a range of V-band surface brightness of 27–31 mag arcsec^{-2}, which corresponds to an r-band magnitude of 26.6–30.6 mag arcsec^{-2}, fully consistent with the range of surface brightnesses in the halo of NGC 1316 (26 -30 mag arcsec^{-2}). The Aq-C halo would result from the gradual accretion of many progenitors, and it is characterized by an exponential light profile, as also found in NGC 1316 (see Section 5.1). One of the most luminous substructures in the stellar envelope of NGC 1316 includes the loops L2 and L3, which should be considered as the most recent accreted satellite. It has $g - r = 0.54 \pm 0.01$ mag (see Table 3), which is comparable with those estimated for the galaxies inside the stellar envelope (see Figure 1), which are 0.54 mag $\leqslant g - r \leqslant 0.60$ mag (see Table 1). Its total luminosity in the g band, $L \geqslant 7 \times 10^9 \, L_\odot$, is comparable to those of the two brightest galaxies inside the envelope, NGC 1310 with $3 \times 10^9 \, L_\odot$ and NGC 1316C with $10 \times 10^9 \, L_\odot$ (see Figure 1 and Table 1). The $g - r$ color gradient observed in the stellar envelope of NGC 1316 (see Figure 4) can also be an indication of a metallicity gradient, also consistent with the stellar halo formed by the accretion of small satellites.

The fraction of the total stellar mass in surviving satellites in the Aq-C model is $f_{\mathrm{sat}} = 0.28$, which contributes about 67% to the total mass of the stellar halo (see Table 2 in Cooper et al. 2010). In NGC 1316 we can estimate a lower limit for such a fraction, due to the detection limit of the VST photometry. This could be given by at least all loops clearly detected in the envelope (L1, L2, L3, L6, and L7). The total luminosity of these surviving satellite remnants, given by the sum of each single contribution (see Table 3), is $\sim 2 \times 10^9 \, L_\odot$ in the g band. This is about 7% of the total luminosity of NGC 1316 (see Section 5) and about 13% of the total luminosity of the stellar envelope (see Table 2).

7.3. NGC 1316 versus NGC 1399: Two Giants in Comparison

NGC 1316 is the giant spheroidal galaxy dominating the subgroup in the southwest of the Fornax Cluster (Drinkwater et al. 2001), with an absolute magnitude in the g band of $M_g = -23.16$ mag (see Section 5). It is brighter than NGC 1399, the central cD galaxy of the Fornax Cluster, which has $M_g = -22.93$ mag (Iodice et al. 2016).

The light profiles of the two giant galaxies have a very similar shape (see Figure 8). Except for the difference in the luminosity, the inner parts for both galaxies are well fitted with a de Vaucouleurs law (see Section 5.1). The outer envelope is characterized by an exponential decline, with comparable levels of central surface brightness and scale lengths. In contrast to the very similar surface brightness profiles, the 2D morphologies of NGC 1316 and NGC 1399 are very different. As illustrated in the present paper, as well as discussed in previous works (see Section 2), NGC 1316 is a dusty spheroid, showing evidence for past major and minor interactions, with a significant rotation of stars along its major axis (Arnaboldi et al. 1998; Bedregal et al. 2006). On the other hand, NGC 1399 appears as a "normal," slow rotator, elliptical galaxy, without dust and any sign of recent major gravitational interaction (see Iodice et al. 2016, and references therein).

The stellar envelope of NGC 1399 contributes more than 60% to the total light, and it is in a very diffuse form. In NGC 1316 this component is $\sim 40\%$ of the total light (see Section 5.1), where several discrete structures, remnants of the accreted progenitors, are still visible at the same fainter level of surface brightnesses of the stellar envelope in NGC 1399. In both galaxies, the stellar envelope reaches the intracluster region, including some cluster galaxy members. Most of the galaxies inside the envelope of NGC 1316 are candidate dwarf galaxies, with 0.54 mag $\leqslant g - r \leqslant 0.6$ mag (i.e., 0.76 mag $\leqslant V - I \leqslant 0.79$ mag), plus two brighter barred spiral galaxies, NGC 1310 and NGC 1317 (see Figure 1 and Table 1). On the contrary, the stellar envelope of NGC 1399 hosts several bright early-type galaxies (Iodice et al. 2016) and a vast population of dwarfs, about 65 objects (Mieske et al. 2007; Munoz et al. 2015), with average colors 0.5 mag $\leqslant V - I \leqslant 1.2$ mag.

Close to the center ($R \leqslant 0.'1$), due to the strong dust absorption, NGC 1316 is slightly redder ($g - r \sim 0.85$ mag; see Figure 4) than NGC 1399 ($g - r \sim 0.8$ mag; see Iodice et al. 2016). The main bodies of both galaxies, where the light profiles are well fitted by a de Vaucouleurs law (see Section 5.1), have similar $g - r$ color, ~ 0.7–0.8 mag. On the other hand, in NGC 1316 the outer envelope shows a gradient toward bluer colors, with 0.7 mag $\leqslant g - r \leqslant 0.4$ mag (see Figure 4), while in NGC 1399 the stellar halo is redder, with $g - r \sim 0.8$ mag.

In the framework of the mass assembly within galaxy clusters, the above analysis suggests that NGC 1316 and NGC 1399 trace a different epoch of the formation history for a cD galaxy. In NGC 1316 the central $r^{1/4}$ spheroid and the outer stellar envelope are still forming. NGC 1399 is in a more evolved phase than NGC 1316, but the similarity in the average light distribution and colors between the galaxies may suggest that the central spheroid in NGC 1399 formed by similar processes supposed for NGC 1316, but in an earlier epoch. This is also a further indication that in the formation history of NGC 1316 the pre-merger galaxy could be an early-type object.

In the stellar envelope of NGC 1316 the remnant features of the accreted progenitors are still present; thus, the accretion is ongoing, but the light distribution has already settled with an exponential decline. In NGC 1399 there are no signs of recent interactions, except the very faint bridge of light toward NGC 1387 (Iodice et al. 2016), but the stellar envelope has a comparable exponential decline (same magnitudes and scale length) to that observed in NGC 1316 (see Section 5.1). Therefore, we could suppose a similar formation process for the stellar envelope in both galaxies, but at different epochs. At the present time, the stellar envelope in NGC 1399 is more virialized.

7.4. On a Larger Scale: The Environment of Fornax A versus the Cluster Core

The group of galaxies around Fornax A, at about 1 Mpc to the southwest of the Fornax Cluster, is bound to it and probably infalling toward the cluster center (Drinkwater et al. 2001). The Fornax core and the subgroup centered on Fornax A may lie along a large filamentary structure of dark matter that is collapsing and flowing in toward a common center. The uniform and large coverage of the Fornax Cluster and its subgroup given by the FDS with VST will provide an
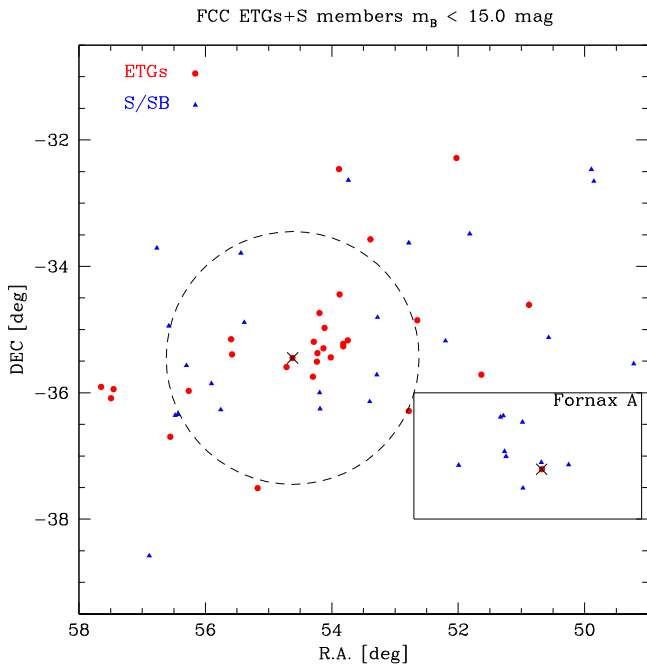
Figure 13. Distribution of early-type (ellipticals and S0s; red circles) and late-type galaxies (blue triangles) in the core of the Fornax Cluster and in the subgroup Fornax A. The two crosses indicate the location of NGC 1399 at the center of the cluster and that of NGC 1316 at the center of the Fornax A subgroup. The dashed circle corresponds to the virial radius $R_{\rm vir} \sim 0.7$ Mpc. The box delimits the region around Fornax A studied in this work and presented in Figure 1.

unprecedented opportunity to study the formation history on the cluster scale. Even if a detailed discussion of this subject is beyond the scope of this paper, it is worth commenting about how the environments around the two cD galaxies (NGC 1399 and NGC 1316) compare, as a complementary discussion to that on the formation history for the two cDs presented in the previous section.

Figure 13 shows all galaxies brighter than $m_B \leqslant 15$ mag from the Fornax Cluster Catalog by Ferguson (1989). Most of the galaxies inside the virial radius of the Fornax Cluster are early-type galaxies, ellipticals, and S0s. The deep VST mosaic of the central 2 square degrees shows that they appear as "normal" spheroids; some of them are barred S0s, with no evident signs of interaction and/or accretion at the lowest magnitudes levels and star-forming regions (Iodice et al. 2016). On the other hand, in the 4 square degrees around NGC 1316 there are only late-type galaxies, barred spirals, and interacting pairs, with luminous knots of active star-forming regions (see Figures 13 and 1). The differences in the environment around NGC 1316 and NGC 1399 are consistent with a different evolutionary epoch claimed above: the subgroup centered on NGC 1316 is in an earlier phase of mass assembly than the core of the cluster, which appears more evolved.

8. Concluding Summary

As part of the FDS with VST, we have obtained a new mosaic of the southwest group of the Fornax Cluster, in the g and r bands, which covers an area of about 3×2 square degrees around the central galaxy NGC 1316 (see Figure 1). The deep photometry, the high spatial resolution of Omega-Cam, and the large covered area allow us, in one shot, to study the galaxy structure, trace stellar halo formation, and look at the

galaxy environment. In particular, we are able to set the scales of the main components dominating the light distribution, which are the central spheroid and the stellar envelope, and to study their properties. We analyzed with great detail the numerous substructures that characterize both components, and the integrated colors derived for each of them turned out to be new important constraints for the formation history of this fascinating galaxy.

NGC 1316 had a rich history of interaction events. There was a "major" gravitational interaction that formed the central spheroid: it could be a major merging of two equal-mass spiral galaxies or an unequal-mass merging of a preexisting early-type disk with a late-type galaxy. We identified the giant SW loop L5 and the smaller and fainter new NW loop L9 as the relics of this process, with a tidal tail of material being expelled during the merger. This claim is based on the similarity between the integrated $g - r$ colors of these features and the average $g - r$ color of the central spheroid. We made a detailed comparison between the global properties observed for NGC 1316 (i.e., morphology, kinematics, and gas content) and those from numerical simulations reproducing the above mergers. The observed properties for the outer tails in NGC 1316 are not reproduced by the disk–disk major merging, and the other proposed scenario (i.e., unequal-mass merging of a preexisting early-type disk with a late-type galaxy) needs to be further investigated. Moreover, we are catching in the act the second phase of the mass assembly, where the accretion of smaller satellites is going on. They are building up the galaxy outskirts and are perturbing the inner structure. In particular, the faint envelope in NGC 1316 still hosts the remnants of the accreted satellite galaxies that are forming the stellar halo. Among them, the most luminous is on the NE of NGC 1316, identified as loops L2 and L3, which have luminosities and colors similar to those of the brightest galaxy members of this subgroup of the Fornax Cluster, inside the envelope. By comparing with cosmological simulations of galactic stellar halo formation, we found that the structure, extensions, light distribution, and mass fraction of the stellar envelope in NGC 1316 are consistent with the stellar halos built up by the gradual accretion of small satellites.

By comparing NGC 1316 with the brightest galaxy in the core of the Fornax Cluster, NGC 1399, we noticed that, even if the structure of the two giants is quite different, the azimuthally averaged surface brightness profiles are surprisingly similar. For both galaxies, the central spheroid has an $\sim r^{1/4}$ behavior, and the outer envelope is characterized by an exponential decline, with a comparable level of central surface brightness and scale lengths. We claimed that, in the framework of the mass assembly within galaxy clusters, NGC 1316 and NGC 1399 trace a different epoch of the formation history for a cD galaxy.

On the cluster scale, the environment around the two giant galaxies is quite different. In the 4 square degrees around NGC 1316 there are only late-types galaxies, with evident signs of interaction and star-forming regions, while most of the galaxies inside the core of the Fornax Cluster are early-type galaxies. Based on this, we suggest a different evolutionary epoch for the two regions of the cluster: the subgroup centered on NGC 1316 is in an earlier phase of mass assembly than the core of the cluster, which appears more evolved.

References

Arnaboldi, M., Freeman, K. C., Gerhard, O., et al. 1998, ApJ, 507, 759
Arnaboldi, M., & Gerhard, O. 2010, HiA, 15, 97
Arnaboldi, M., Ventimiglia, G., Iodice, E., Gerhard, O., & Coccato, L. 2012, A&A, 545, A37
Balcells, M. 1997, ApJL, 486, L87
Barnes, J. E. 1992, ApJ, 393, 484
Bassino, L. P., Faifer, F. R., Forte, J. C., et al. 2006, A&A, 451, 789
Bedregal, A. G., Aragón-Salamanca, A., Merrifield, M. R., & Milvang-Jensen, B. 2006, MNRAS, 371, 1912
Beletsky, Y., Gadotti, D. A., Moiseev, A., Alves, J., & Kniazev, A. 2011, MNRAS, 418, L6
Cantiello, M., Grado, A., Blakeslee, J. P., et al. 2013, A&A, 552, A106
Caon, N., Capaccioli, M., & D'Onofrio, M. 1994, A&AS, 106, 199
Capaccioli, M., Spavone, M., Grado, A., et al. 2015, A&A, 581, A10
Carlqvist, P. 2010, Ap&SS, 327, 267
Chilingarian, I. V., Di Matteo, P., Combes, F., Melchior, A.-L., & Semelin, B. 2010, A&A, 518, A61
Contini, E., De Lucia, G., Villalobos, Á, & Borgani, S. 2014, MNRAS, 437, 3787
Cooper, A. P., Cole, S., Frenk, C. S., et al. 2010, MNRAS, 406, 744
Cooper, A. P., D'Souza, R., Kauffmann, G., et al. 2013, MNRAS, 434, 3348
Cooper, A. P., Gao, L., Guo, Q., et al. 2015a, MNRAS, 451, 2703
Cooper, A. P., Parry, O. H., Lowing, B., Cole, S., & Frenk, C. 2015b, MNRAS, 454, 3185
Crnojević, D., Sand, D. J., Spekkens, K., et al. 2016, ApJ, 823, 19
Cui, W., Murante, G., Monaco, P., et al. 2014, MNRAS, 437, 816
D'Abrusco, R., Cantiello, M., Paolillo, M., et al. 2016, ApJL, 819, L31
De Lucia, G., & Blaizot, J. 2007, MNRAS, 375, 2
Donzelli, C. J., Muriel, H., & Madrid, J. P. 2011, ApJS, 195, 15
Drinkwater, M. J., Gregg, M. D., & Colless, M. 2001, ApJL, 548, L139
Duah Asabere, B., Horellou, C., Jarrett, T. H., & Winkler, H. 2016, A&A, 592, A20
Duc, P.-A., Cuillandre, J.-C., Karabal, E., et al. 2015, MNRAS, 446, 120
Ekers, R. D., Goss, W. M., Wellington, K. J., et al. 1983, A&A, 127, 361
Fabbiano, G., Kim, D.-W., & Trinchieri, G. 1992, ApJS, 80, 531
Feigelson, E. D., Laurent-Muehleisen, S. A., Kollgaard, R. I., & Fomalont, E. B. 1995, ApJL, 449, L149
Ferguson, H. C. 1989, AJ, 98, 367
Ferrarese, L., Côté, P., Cuillandre, J.-C., et al. 2012, ApJS, 200, 4
Fomalont, E. B., Ebneter, K. A., van Breugel, W. J. M., & Ekers, R. D. 1989, ApJL, 346, L17

Fukugita, M., Ichikawa, T., Gunn, J. E., et al. 1996, AJ, 111, 1748
Geldzahler, B. J., & Fomalont, E. B. 1984, AJ, 89, 1650
Goudfrooij, P. 2012, ApJ, 750, 140
Goudfrooij, P., Alonso, M. V., Maraston, C., & Minniti, D. 2001, MNRAS, 328, 237
Grado, A., Capaccioli, M., Limatola, L., & Getman, F. 2012, MSAIS, 19, 362
Grillmair, C. J., Freeman, K. C., Bicknell, G. V., et al. 1994, ApJL, 422, L9
Hernquist, L., & Spergel, D. N. 1992, ApJL, 399, L117
Hilker, M. 2015, IAUGA, 22, 2215712
Horellou, C., Black, J. H., van Gorkom, J. H., et al. 2001, A&A, 376, 837
Huang, S., Ho, L. C., Peng, C. Y., Li, Z.-Y., & Barth, A. J. 2013, ApJ, 766, 47
Iodice, E., Capaccioli, M., Grado, A., et al. 2016, ApJ, 820, 42
Iyomoto, N., Makishima, K., Tashiro, M., et al. 1998, ApJL, 503, L31
James, F., & Roos, M. 1975, CoPhC, 10, 343
Janowiecki, S., Mihos, J. C., Harding, P., et al. 2010, ApJ, 715, 972
Jordán, A., Blakeslee, J. P., Côté, P., et al. 2007, ApJS, 169, 213
Kim, D. W., & Fabbiano, G. 2003, ApJ, 586, 826
Kim, D. W., Fabbiano, G., & Mackie, G. 1998, ApJ, 497, 699
Konami, S., Matsushita, K., Nagino, R., et al. 2010, PASJ, 62, 1435
Kuijken, K. 2011, Msngr, 146, 8
Lanz, L., Jones, C., Forman, W. R., et al. 2010, ApJ, 721, 1702
Mackie, G., & Fabbiano, G. 1998, AJ, 115, 514
Martel, H., Barai, P., & Brito, W. 2012, ApJ, 757, 48
Martínez-Delgado, D., Gabany, R. J., Crawford, K., et al. 2010, AJ, 140, 962
McNeil-Moylan, E. K., Freeman, K. C., Arnaboldi, M., & Gerhard, O. E. 2012, A&A, 539, A11
Merritt, A., van Dokkum, P., Abraham, R., & Zhang, J. 2016, ApJ, 830, 62
Mieske, S., Hilker, M., Infante, L., & Mendes de Oliveira, C. 2007, A&A, 463, 503
Mihos, C. 2015, IAUGA, 22, 2247903
Mihos, J. C., Harding, P., Feldmeier, J., & Morrison, H. 2005, ApJL, 631, L41
Mihos, J. C., Harding, P., Feldmeier, J. J., et al. 2016, arXiv:1611.04435
Mihos, J. C., & Hernquist, L. 1996, ApJ, 464, 641
Munoz, R. P., Eigenthaler, P., & Puzia, T. H. e. a. 2015, ApJL, 813, L15
Napolitano, N. R., Pannella, M., Arnaboldi, M., et al. 2003, ApJ, 594, 172
Oser, L., Ostriker, J. P., Naab, T., Johansson, P. H., & Burkert, A. 2010, ApJ, 725, 2312
Pillepich, A., Vogelsberger, M., Deason, A., et al. 2014, MNRAS, 444, 237
Puchwein, E., Springel, V., Sijacki, D., & Dolag, K. 2010, MNRAS, 406, 936
Quinn, P. J. 1984, ApJ, 279, 596
Ricciardelli, E., Vazdekis, A., Cenarro, A. J., & Falcón-Barroso, J. 2012, MNRAS, 424, 172
Richtler, T., Bassino, L. P., Dirsch, B., & Kumar, B. 2012, A&A, 543, A131
Richtler, T., Hilker, M., Kumar, B., et al. 2014, A&A, 569, A41
Rodriguez-Gomez, V., Pillepich, A., Sales, L. V., et al. 2016, MNRAS, 458, 2371
Roediger, J. C., Courteau, S., MacArthur, L. A., & McDonald, M. 2011, MNRAS, 416, 1996
Scharf, C. A., Zurek, D. R., & Bureau, M. 2005, ApJ, 633, 154
Schipani, P., Noethe, L., Arcidiacono, C., et al. 2012, JOSAA, 29, 1359
Schlegel, D. J., Finkbeiner, D. P., & Davis, M. 1998, ApJ, 500, 525
Schuberth, Y., Richtler, T., Hilker, M., et al. 2010, A&A, 513, A52
Schulz, C., Hilker, M., Kroupa, P., & Pflamm-Altenburg, J. 2016, A&A, 594, A119
Schweizer, F. 1980, ApJ, 237, 303
Seigar, M. S., Graham, A. W., & Jerjen, H. 2007, MNRAS, 378, 1575
Sesto, L. A., Faifer, F. R., & Forte, J. C. 2016, MNRAS, 461, 4260
Spavone, M., Capaccioli, M., Napolitano, N. R., et al. 2017, A&A, in press (arXiv:1703.10835)
Trujillo, I., & Fliri, J. 2016, ApJ, 823, 123
Tutukov, A. V., & Fedorova, A. V. 2011, ARep, 55, 383
van Dokkum, P. G., Abraham, R., & Merritt, A. 2014, ApJL, 782, L24
Vazdekis, A., Ricciardelli, E., Cenarro, A. J., et al. 2012, MNRAS, 424, 157
Watson, D. F., Berlind, A. A., & Zentner, A. R. 2012, ApJ, 754, 90